Stem Cell Reports
Article
ISSCR
OPEN ACCESS

MeCP2 and Major Satellite Forward RNA Cooperate for Pericentric Heterochromatin Organization

Salvatore Fioriniello,[1] Eva Csukonyi,[1] Domenico Marano,[1] Arianna Brancaccio,[1] Michele Madonna,[2] Carmela Zarrillo,[1] Alessia Romano,[3] Federico Marracino,[2] Maria R. Matarazzo,[1] Maurizio D'Esposito,[1] and Floriana Della Ragione[1,*]

[1]Institute of Genetics and Biophysics 'A. Buzzati-Traverso', CNR, Naples 80131, Italy
[2]IRCCS Neuromed, Pozzilli (Is) 86077, Italy
[3]CEINGE-Biotecnologie Avanzate, Naples 80131, Italy
*Correspondence: floriana.dellaragione@igb.cnr.it
https://doi.org/10.1016/j.stemcr.2020.11.006

SUMMARY

Methyl-CpG binding protein 2 (MeCP2) has historically been linked to heterochromatin organization, and in mouse cells it accumulates at pericentric heterochromatin (PCH), closely following major satellite (*MajSat*) DNA distribution. However, little is known about the specific function of MeCP2 in these regions. We describe the first evidence of a role in neurons for MeCP2 and *MajSat* forward (*MajSat-fw*) RNA in reciprocal targeting to PCH through their physical interaction. Moreover, MeCP2 contributes to maintenance of PCH by promoting deposition of H3K9me3 and H4K20me3. We highlight that the MeCP2B isoform is required for correct higher-order PCH organization, and underline involvement of the methyl-binding and transcriptional repression domains. The T158 residue, which is commonly mutated in Rett patients, is directly involved in this process. Our findings support the hypothesis that MeCP2 and the *MajSat-fw* transcript are mutually dependent for PCH organization, and contribute to clarify MeCP2 function in the regulation of chromatin architecture.

INTRODUCTION

Since its identification (Lewis et al., 1992), the number of biological functions ascribed to methyl-CpG binding protein 2 (MeCP2) has grown exponentially. The X-linked *MECP2* gene is mutated in 95% of patients with Rett syndrome (RTT; OMIM 312750) (Amir et al., 1999; D'Esposito et al., 1996; Rett, 1966), a severe neurodevelopmental disease that affects mainly female individuals. Expression of MeCP2 increases during neuronal differentiation (Jung et al., 2003). Constitutive and brain-specific ablation of *Mecp2* in mouse reproduces the RTT phenotypes and highlights the importance of MeCP2 for brain function (Guy et al., 2001).

The *MECP2* gene encodes two splicing isoforms that are highly expressed in brain: MeCP2A and MeCP2B. These both have a methyl-binding domain (MBD) and a transcriptional repression domain (TRD), which, in turn, contains the NCoR/SMRT interaction domain (NID); they differ in terms of their N-terminus (Della Ragione et al., 2016). These MeCP2 isoforms show similar nuclear localization (Kumar et al., 2008); however, MeCP2B is the predominant form expressed in brain (Dragich et al., 2007) and appears to be relevant for RTT pathogenesis (Gianakopoulos et al., 2012). Moreover, MeCP2A and MeCP2B bind unique partners and show different genomic binding site preferences (Martinez de Paz et al., 2019).

The main function of MeCP2 has been linked to DNA methylation-mediated transcriptional repression (Klose and Bird, 2003), although it also activates gene expression in specific brain regions (Ben-Shachar et al., 2009; Chahrour et al., 2008). Multiple roles of MeCP2 might be due to interactions with different molecular partners (for review, see Della Ragione et al., 2016), such as histone deacetylases and switch-independent 3A (Sin3A) for transcriptional repression, or cAMP response element-binding protein (CREB 1) for gene activation.

MeCP2 has a role in genome-wide transcriptional silencing. In mouse neurons, it is important for repression of spurious transcription of repetitive elements, and its genomic binding tracks the methyl-CpG distribution (Skene et al., 2010). In mouse cells, MeCP2 accumulates at pericentric heterochromatin (PCH) (Lewis et al., 1992), which is constitutive heterochromatin organized in higher-order chromatin structures, known as chromocenters. These originate from aggregation of PCH of different chromosomes, undergo dynamic reorganization during differentiation, and are visible using DAPI staining (Almouzni and Probst, 2011). PCH is involved in repression of transposons, chromosomal segregation, genome integrity, and *in-cis* and *in-trans* silencing of euchromatic genes. In mouse, PCH is composed of hypermethylated 234-bp major satellite (*MajSat*) AT-rich repeats, which form complexes with hypo-acetylated and trimethylated histones H3 and H4 (e.g., H3K9me3, H4K20me3). These histones, in turn, promote anchoring of specific factors, such as members of the heterochromatin protein 1 (HP1) family and the cohesin complex, respectively (Fioriniello et al.,

2020). The interactions between PCH regions appear to promote genomic compartmentalization in the nucleus (Falk et al., 2019), and recent findings support the importance of PCH in the formation of repressive compartments where silenced genes are positioned (Wijchers et al., 2015). However, whether MeCP2 directly regulates this process remains unclear. MeCP2 mediates chromocenter clustering during both myogenic and neural differentiation, with the contribution of α-thalassemia/mental retardation syndrome X-linked protein (ATRX) (Bertulat et al., 2012; Brero et al., 2005; Marano et al., 2019).

Interestingly, a role for RNAs in higher-order PCH organization has been highlighted (Maison et al., 2002, 2011; Marano et al., 2019; Park et al., 2018). Moreover, noncoding RNAs (ncRNAs) of heterogeneous lengths from both strands of *MajSat* DNA have been detected (Lehnertz et al., 2003), despite the heterochromatic nature of this genomic region. However, their biological significance remains unclear. *MajSat* RNA levels increase during neuronal differentiation in the developing mouse brain (Kishi et al., 2012). Also, they participate in the recruitment to PCH of scaffold attachment factor B (SAFB) (Huo et al., 2020) and suppressor of variegation 3-9 homolog (Suv39h), the enzyme responsible for trimethylation of H3K9 (Velazquez Camacho et al., 2017), and they have roles in chromocenter condensation during myogenic differentiation (Park et al., 2018). Moreover, at the two-cell stage during early mouse development, *MajSat* transcripts are crucial for developmental progression and formation of chromocenters. The functions of the two strands appear to be independent (Casanova et al., 2013; Probst et al., 2010), and the forward transcript (*MajSat-fw*) is directly involved in *de novo* targeting of small ubiquitin-like modifier (SUMO)-modified HP1α to PCH (Maison et al., 2011). Whether *MajSat* RNAs or other RNA components cooperate with MeCP2 for PCH organization is still elusive.

Here, we investigated the role of *MajSat* RNAs in MeCP2-mediated higher-order PCH organization in neurons. Furthermore, we dissected out the specific role of the MeCP2A and MeCP2B isoforms in this process, as well as the contribution of the MBD and TRD domains. Finally, we examined whether two common RTT mutations, T158M and R306C, affect PCH organization.

RESULTS

MeCP2 Binding to Chromocenters Is Dependent on RNA Components

To determine whether an RNA component promotes accumulation of MeCP2 at PCH in neurons, we used TK23 wild-type (TK23_WT) and MeCP2 deficient (*Mecp2*$^{-/y}$ tEG; here as *Mecp2*$^{-/y}$) murine embryonic stem cells (mESCs), which were previously used to demonstrate the role for MeCP2 in chromocenter clustering (Bertulat et al., 2012). Neural differentiation of these cells gives rise to a cell population that is enriched in neurons and astroglia (Bertulat et al., 2012; Fico et al., 2008) (Figure 1A). Immunofluorescence performed after RNase A treatment on terminally differentiated TK23_WT neurons showed that MeCP2 is dispersed in the nucleus, and thus loses its usual PCH accumulation, which was seen for only 2.5% of the nuclei. Conversely, in mock-treated TK23_WT neurons, the majority of the nuclei (98.5%) showed strong spotting of MeCP2 at chromocenters, as expected (Figure 1B). Of note, the dense DAPI staining that corresponds to chromocenters was still visible.

MeCP2 strongly binds *MajSat* DNA in mESC-derived TK23_WT neurons, as shown by chromatin immunoprecipitation (ChIP); however, RNase A treatment displaced MeCP2 from these genomic regions (Figure 1C), thus confirming the immunofluorescence data. These findings suggest that an RNA component contributes to the recruitment of MeCP2 to PCH in mESC-derived neurons.

MeCP2 Contributes to Major Satellite Forward Transcript Targeting to Chromocenters

MajSat ncRNAs represent ideal candidates for molecular partners of MeCP2 (Casanova et al., 2013; Maison et al., 2011; Park et al., 2018). We first analyzed the expression of both forward and reverse *MajSat* (*MajSat-fw*, *MajSat-rv*, respectively) RNAs by qPCR after strand-specific reverse transcription (RT-qPCR) in terminally differentiated TK23_WT and *Mecp2*$^{-/y}$ neurons. *MajSat-fw* and *MajSat-rv* RNAs were both expressed in TK23_WT and *Mecp2*$^{-/y}$ neurons, without any significant differences between these two cell lines (Figure 2A, top). Moreover, the RT-qPCR products of both *MajSat-fw* and *MajSat-rv* RNAs had different lengths (Figure 2A, bottom), which suggested the expression of multiple repeated units, as previously reported in other cellular contexts (Maison et al., 2011).

We next analyzed the nuclear localization of *MajSat* RNAs in both the TK23_WT and *Mecp2*$^{-/y}$ undifferentiated cells and in the neurons, using interphase three-dimensional (i3D)-RNA fluorescence *in situ* hybridization (FISH) with strand-specific locked nucleic acid (LNA) probes. In the undifferentiated cells, the *MajSat-fw* transcripts were visible as small nuclear spots in both cell lines, and were not detected after RNase A treatment, which ruled out cross-reactions with DNA. However, the number of *MajSat-fw* RNA signals/nucleus was significantly greater in TK23_WT nuclei compared with *Mecp2*$^{-/y}$ nuclei (Figure 2B), even though the expression of *MajSat-fw* RNA was similar in the two cell lines (Figure S1A).

Following the neural differentiation, the sizes and numbers of *MajSat-fw* RNA signals were increased in both TK23_WT and *Mecp2*$^{-/y}$ neurons (Figure 2C), compared

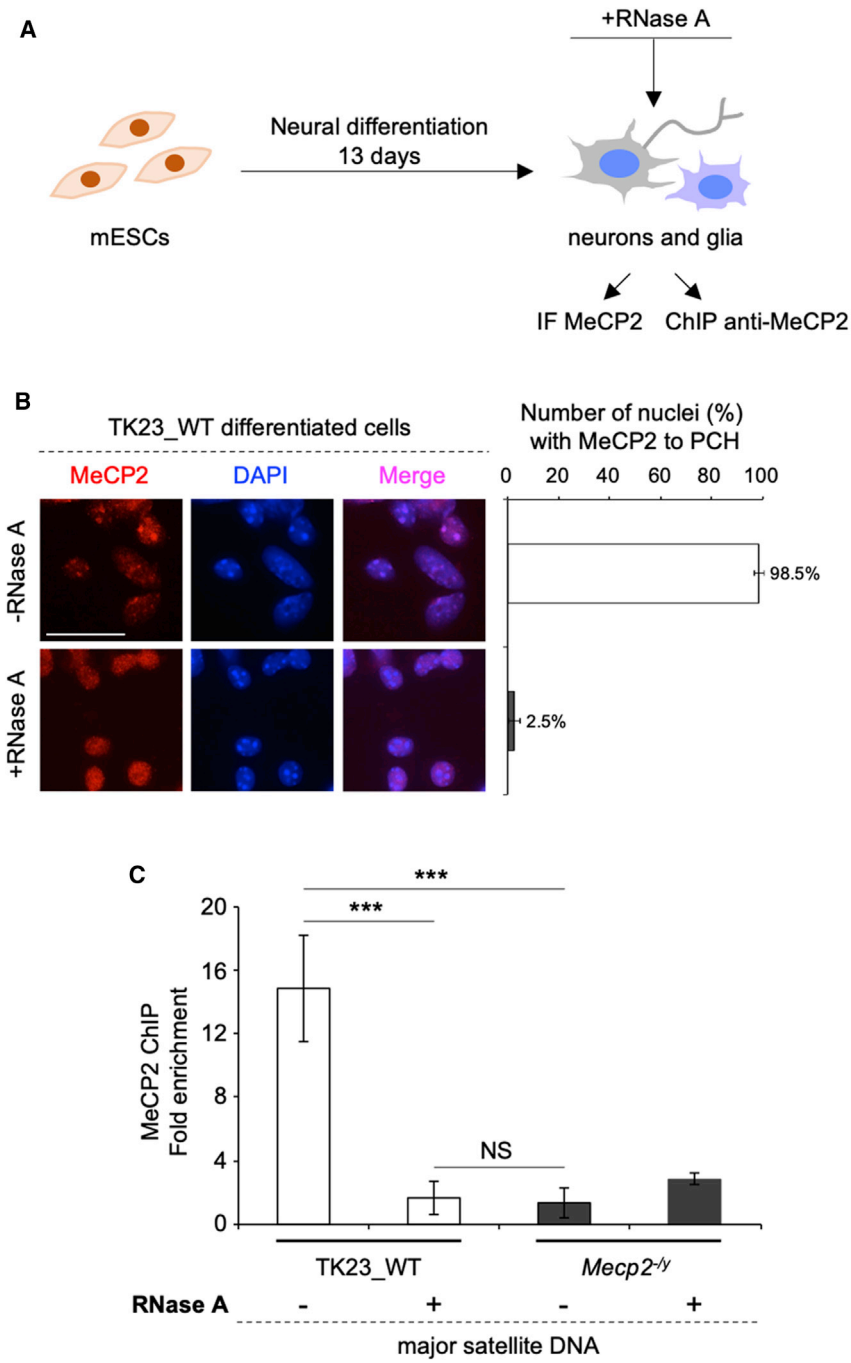

Figure 1. MeCP2 Accumulation at PCH Depends on an RNA Component

(A) Scheme of the experimental procedure.

(B) Left: Representative immunofluorescence of MeCP2 in terminally differentiated TK23_WT neurons without and with RNase A treatment. Chromocenters were stained with DAPI. Scale bar, 25 μm. Right: Quantification of MeCP2 enrichment at chromocenters without and with RNase A treatment. Data are means ± SD, with ≥100 cells analyzed per condition, from two independent experiments.

(C) ChIP–qPCR of MeCP2 at *MajSat* DNA in mESC-derived *Mecp2*$^{-/y}$ (negative control) and TK23_WT neurons without and with RNase A treatment. Data are means ± SD of four independent qPCR replicates from two ChIP experiments. ***p < 0.001; NS, not significant (one-tailed Student's t test).

with undifferentiated cells (Figure 2B), and in both cell lines they were associated with chromocenters. Furthermore, the number of signals was significantly greater for TK23_WT neurons compared with *Mecp2*$^{-/y}$ neurons, and when the images were captured under constant image-acquisition parameters, the RNA signals for *Mecp2*$^{-/y}$ nuclei appeared less bright compared to TK23_WT nuclei (Figure 2C).

Interphase three-dimensional-RNA FISH performed at an early differentiation stage (day 8) showed spatial distribution of the *MajSat-fw* transcripts similar to that for the terminally differentiated neurons, with significantly greater numbers of signals in the TK23_WT cells (Figure S1B). Moreover, comparison of the number of RNA signals/nucleus over the three time points analyzed showed a gradual increase in both TK23_WT and *Mecp2*$^{-/y}$ cells (Figure S1C),

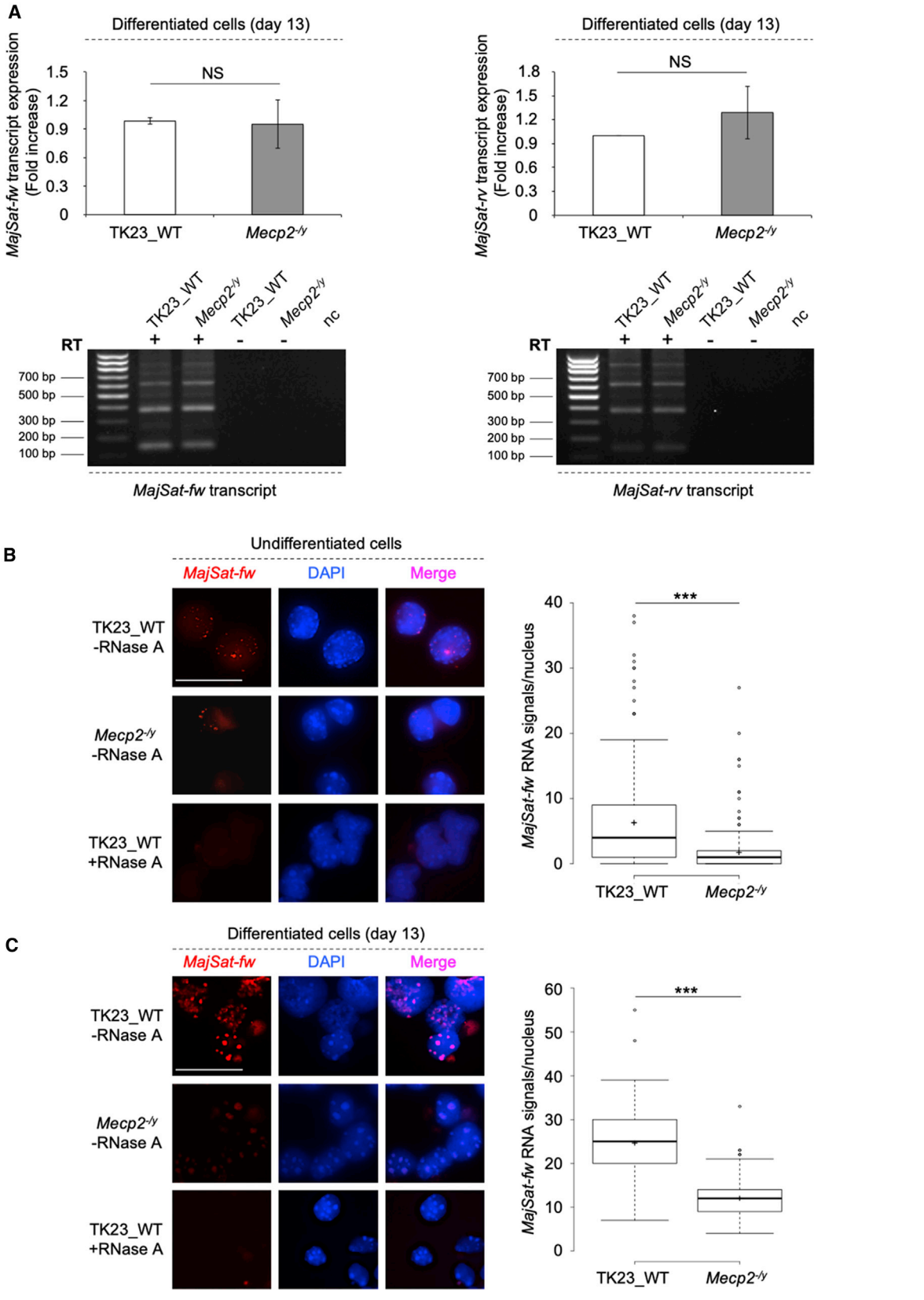

(legend on next page)

which suggested progressive accumulation of the transcript at the chromocenters during neural differentiation.

Altogether, these findings let us hypothesize a remarkable contribution of MeCP2 in *MajSat-fw* transcript targeting to PCH during neural differentiation.

In contrast with the *MajSat-fw* transcript, the *MajSat-rv* RNA did not show any accumulation as fluorescent spots in the TK23_WT or the *Mecp2*$^{-/y}$ undifferentiated and differentiated cells (Figure S1D), although its expression was detected in both of these cell lines (Figure 2A).

MeCP2 Associates with the *MajSat-fw* Transcript to Chromocenters and Physically Interacts with It

The reciprocal nuclear localization of MeCP2 and *MajSat-fw* RNA was assayed by immuno-RNA FISH in TK23_WT cells. In undifferentiated cells, the *MajSat-fw* transcript was localized to the periphery of the chromocenters, where MeCP2 strongly accumulated. In terminally differentiated TK23_WT neurons, the number of *MajSat-fw* RNA signals was greater and partially colocalized with the MeCP2 signals to chromocenters (Figure 3A). Furthermore, native RNA immunoprecipitation (RIP) carried out on mESC-derived TK23_WT neurons revealed physical interactions between MeCP2 and the *MajSat* transcripts. Conversely, binding of *metastasis-associated lung-adenocarcinoma transcript 1* (*MALAT1*) (which shows weak binding with MeCP2 in cerebellum; Maxwell et al., 2013), was comparable between the TK23_WT and negative control neurons (Figure 3B), which confirmed the specificity of this binding. Similar data were obtained in total brain of WT mice, even though weak binding of MeCP2 with the *MALAT1* transcript was detected (Figure 3C).

We further confirmed a direct interaction between MeCP2 and *MajSat-fw* transcript in terminally differentiated neurons by fluorescence resonance energy transfer (FRET). Here, we carried out RNA FISH to specifically label the *MajSat-fw* transcript with an LNA probe in mESC-derived *Mecp2*[WT]^{EGFP} (referred to as WT-GFP) neurons expressing endogenous MeCP2 fused with EGFP at its C-terminus (Lyst et al., 2013). This assay demonstrated that the donor EGFP conjugated to MeCP2 and the acceptor TYE563, which labels *MajSat-fw* LNA, are in close proximity (Figure S2).

Altogether, these findings highlight the highly specific binding of MeCP2 to the *MajSat* transcripts in neurons, both *in vitro* and *in vivo*, in agreement with the immuno-RNA FISH data.

MajSat-fw Transcript Contributes to MeCP2 Targeting to PCH

To understand whether the *MajSat-fw* transcript is required for targeting of MeCP2 to PCH (see Figure 1), we silenced this ncRNA in mESC-derived TK23_WT neurons by transfection of a specific antisense LNA gapmer (Figure 4A). First, we verified that mESC-derived neurons can be transfected with gapmers (Figure S3A), and then we optimized the protocol to efficiently knock-down *MajSat-fw* RNA in mESC-derived TK23_WT neurons (Figures 4B and S3B). Here, 300 nM *MajSat-fw* gapmer was sufficient to deplete ~80% of the *MajSat-fw* transcript, without any effects on *MajSat-rv* transcript levels (Figure 4B). Immunofluorescence carried out in terminally differentiated TK23_WT neurons transfected with the *MajSat-fw* gapmer showed that MeCP2 was located to chromocenters in <40% of the nuclei, while, in the rest of the nuclei, the majority of MeCP2 signals were widespread in the nucleoplasm. Conversely, in TK23_WT neurons transfected with the negative control gapmer, MeCP2 was strongly accumulated at PCH (Figure 4C). These data were confirmed by ChIP in terminally differentiated TK23_WT neurons, which showed ~50% lower MeCP2 binding to *MajSat* DNA after *MajSat-fw* RNA knock-down (Figure 4D). Of note, major satellite DNA repeats were similarly hypermethylated in TK23_WT neurons transfected with either the *MajSat-fw* or the negative control gapmer (Figure S3C), which suggests that the reduced accumulation of MeCP2 at PCH is not a result of loss of DNA methylation.

Overall, these data highlighted a specific contribution of the *MajSat-fw* transcript in the targeting of MeCP2 to chromocenters in mESC-derived neurons.

MeCP2 Contributes to the Organization of PCH Architecture by Preserving the Correct Deposition of H3K9me3 and H4K20me3

To understand the role of MeCP2 in the global organization of PCH, we analyzed the nuclear distribution of H3K9me3

Figure 2. MeCP2 Has a Role in *MajSat* Forward Transcript Targeting to PCH

(A) Top: Strand-specific RT-qPCR analysis of *MajSat-fw* and *MajSat-rv* transcripts in mESC-derived TK23_WT and *Mecp2*$^{-/y}$ neurons. Data are normalized to *Gapdh* and are means ± SD of transcript levels relative to TK23_WT, from three independent experiments. NS, not significant (two-tailed Student's t test). Bottom: Electrophoretic analyses of endpoint strand-specific RT-qPCR for the *MajSat-fw* and *MajSat-rv* RNAs. RT, reverse transcriptase; nc, negative control. (B, C) Left: Representative images of i3D-RNA FISH using the *MajSat-fw* LNA probe in TK23_WT and *Mecp2*$^{-/y}$ undifferentiated cells (B) and mESC-derived neurons (C) without and with RNase A treatment. Chromocenters were stained with DAPI. Scale bar, 25 μm. Right: Quantification of *MajSat-fw* RNA signals in the three-dimensional space of each nucleus. Data are shown as box and whisker plots with 200 nuclei analyzed per condition, from two replicate slides. ***p < 0.001 (two-sample Kolmogorov-Smirnov test). See also Figure S1.

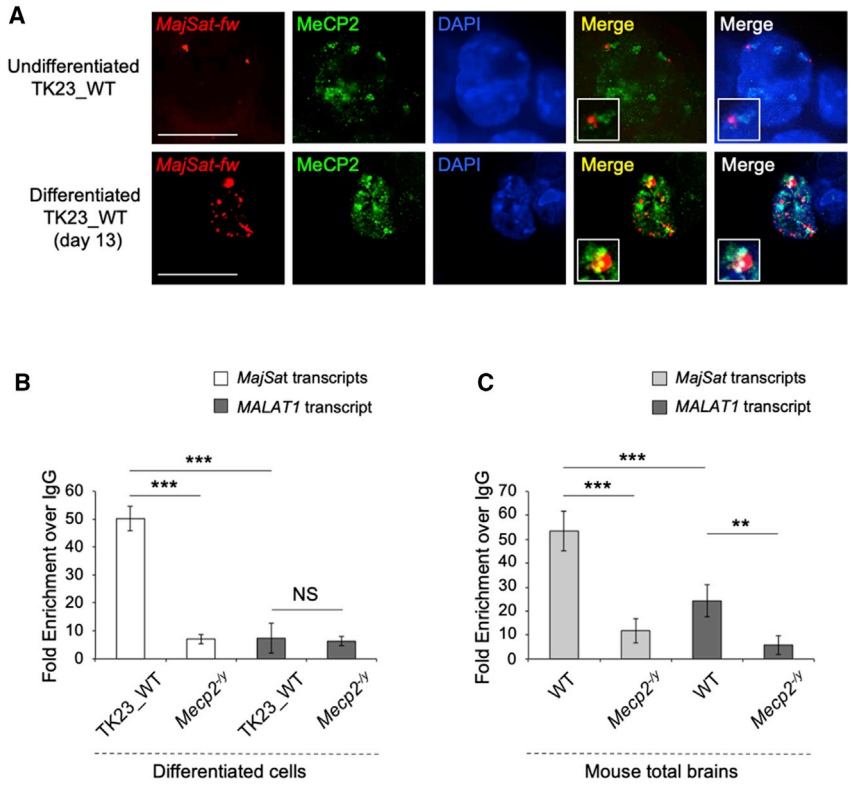

Figure 3. MeCP2 Spatially and Physically Interacts with the *MajSat* Transcripts

(A) Representative images of undifferentiated TK23_WT cells and mESC-derived TK23_WT neurons examined by immuno-RNA FISH using *MajSat-fw* LNA probe and anti-MeCP2 antibody. Chromocenters were stained with DAPI. Merge: MeCP2/*MajSat-fw* RNA signals and MeCP2/*MajSat-fw* RNA/DAPI signals. Insets show magnifications of a chromocenter. Scale bar, 15 μm.

(B and C) RNA immunoprecipitation of *MajSat* transcripts in mESC-derived *Mecp2*$^{-/y}$ (negative control) and TK23_WT neurons (B), and in total brain from *Mecp2*$^{-/y}$ (negative control) and WT mice (C), using an anti-MeCP2 antibody.

Data are means ± SD of four independent qPCR replicates from two RIP experiments. ***p < 0.001; **p < 0.01; NS, not significant (one-tailed Student's t test). See also Figure S2.

and H4K20me3 in terminally differentiated TK23_WT and *Mecp2*$^{-/y}$ neurons. These repressive histone modifications appeared to predominantly accumulate at chromocenters in both of these cell lines. However, quantitative analysis performed by counting the fractions of the nuclei that showed H3K9me3 spotted to chromocenters highlighted a slightly, but significantly, lower proportion (~10%) of spotted nuclei in *Mecp2*$^{-/y}$ compared with TK23_WT neurons. The same analysis performed for H4K20me3 did not show any significant differences (Figure 5A); however, ChIP assays, which are a more sensitive and quantitative method, highlighted remarkably lower (~50%) accumulation of both histone marks at *MajSat* DNA in the absence of MeCP2 (Figure 5B), despite their unchanged protein levels (Figure 5C).

These data demonstrated that MeCP2 has a role in correct deposition of the H3K9me3 and H4K20me3 marks to PCH in terminally differentiated neurons, thus contributing to the organization of PCH architecture.

MeCP2B Rescues Chromocenter Clustering during Neural Differentiation and Contributes to *MajSat-fw* Transcript Targeting to PCH

We previously highlighted a key role for MeCP2 in chromocenter clustering during neural differentiation (Bertulat et al., 2012). Furthermore, we have here revealed a reciprocal contribution of MeCP2 and *MajSat-fw* RNA for their targeting to PCH. Next, we asked which MeCP2 isoform is responsible for this higher-order PCH organization, and what are the contributions of their two main domains, MBD and TRD.

Starting from the *Mecp2*$^{-/y}$ mESCs, we generated stable clones that selectively and constitutively expressed MeCP2A (*Mecp2*$^{-/y}$_MeCP2A) or MeCP2B (*Mecp2*$^{-/y}$_MeCP2B), and also MeCP2B lacking MBD (*Mecp2*$^{-/y}$_MeCP2B_ΔMBD) or TRD (*Mecp2*$^{-/y}$_MeCP2B_ΔTRD) (Figures S4 and S5). MBD or TRD were deleted from MeCP2B because in the brain it is 10-fold more abundant than MeCP2A (Kriaucionis and Bird, 2004).

As the subsequent experiments were performed in differentiated cells, we selected the mESC clones that showed MeCP2 protein levels comparable with those of the TK23_WT neurons (Figures S4A, S4B, S5A, and S5B) and, then, we confirmed their differentiation toward a neural fate (Figures S4C and S5C). Moreover, side-by-side comparison of MeCP2 protein levels in all of these selected clones confirmed their similar expression (Figure S6A).

To investigate which isoform and which domain of MeCP2 is involved in chromocenter clustering, we performed i3D-DNA FISH in the selected clones, in comparison with TK23_WT and *Mecp2*$^{-/y}$ cells, at days 0 (undifferentiated cells) and 13 of neural differentiation.

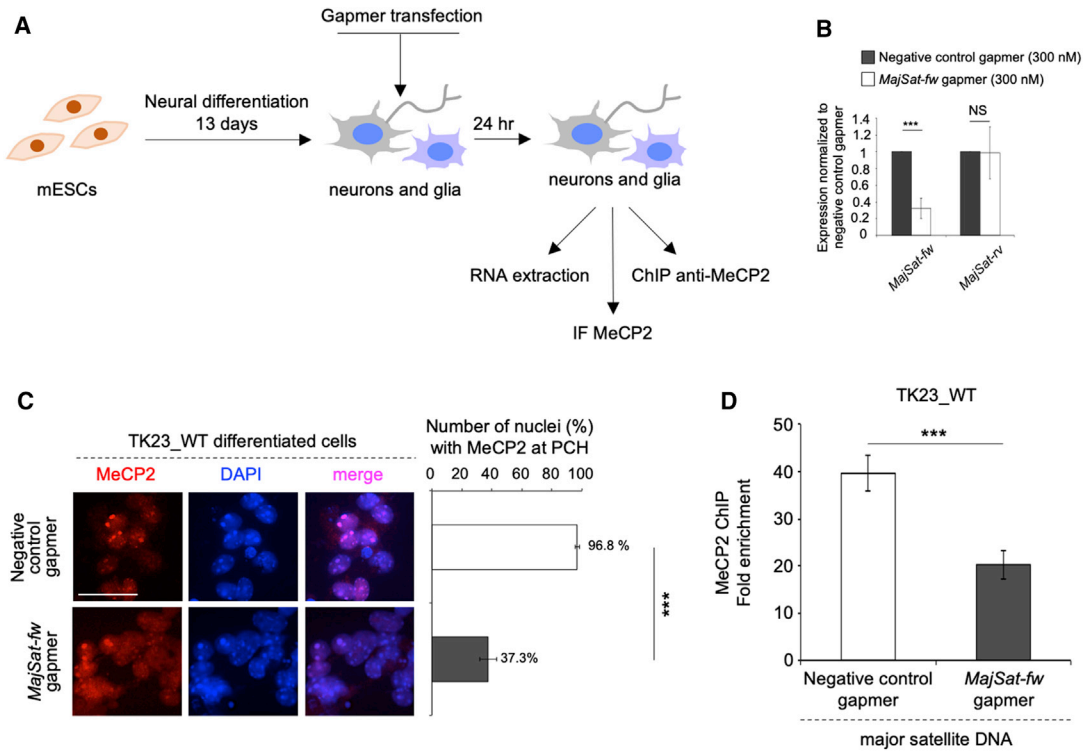

Figure 4. MeCP2 Targeting to Chromocenters Is Partly Dependent on the *MajSat-fw* Transcript

(A) Scheme of the experimental procedure.

(B) Strand-specific RT-qPCR analysis of *MajSat-fw* and *MajSat-rv* transcripts in mESC-derived TK23_WT neurons transfected with 300 nM negative control or *MajSat-fw* gapmers. Data are normalized to *Gapdh* and are means ± SD of transcript levels relative to cells transfected with negative control gapmer, from three biological replicates, with each amplified twice. ***p < 0.001; NS, not significant (one-tailed Student's t test).

(C) Left: Representative immunofluorescence of MeCP2 in mESC-derived TK23_WT neurons transfected with negative control or *MajSat-fw* gapmers. Chromocenters were stained with DAPI. Scale bar, 25 μm. Right: Quantification of MeCP2 enrichment at PCH following transfection of negative control or *MajSat-fw* gapmers. Data are means ± SD, with ≥100 cells analyzed per condition, from four independent experiments. ***p < 0.001 (one-tailed Student's t test).

(D) ChIP–qPCR of MeCP2 at *MajSat* DNA in mESC-derived TK23_WT neurons transfected with negative control or *MajSat-fw* gapmers. Data are means ± SD of four independent qPCR replicates from two ChIP experiments. ***p < 0.001; NS, not significant (one-tailed Student's t test). See also Figure S3.

Chromocenters were detected using the *MajSat-fw* LNA probe, which can reveal even small differences. We found that the *MajSat* DNA distribution overlapped with the intense DAPI staining in the nuclei of all of the cell lines. Chromocenter clustering was evaluated in each cell line by comparing the number of chromocenters at days 0 and 13. We highlighted significantly fewer chromocenters/nucleus in each cell line at day 13 in comparison with day 0, due to aggregation of chromocenters (clustering), although to different extents (Figures 6A–6F).

To highlight possible defects in chromocenter clustering, we compared the number of chromocenters/nucleus among the different cell lines as the terminally differentiated neurons. In comparison with TK23_WT neurons, *Mecp2*$^{-/y}$ neurons showed impaired chromocenter clustering, as previously reported (Bertulat et al., 2012). *Mecp2*$^{-/y}$_MeCP2A neurons showed a partial rescue of the chromocenter clustering, whereas MeCP2B expression completely recovered PCH condensation (Figure 6G), which suggested a prominent role of MeCP2B in chromocenter clustering. Interestingly, *Mecp2*$^{-/y}$_MeCP2B_ΔMBD neurons showed a defect in chromocenter clustering similar to that of *Mecp2*$^{-/y}$_MeCP2A neurons, whereas MeCP2B_ΔTRD expression induced complete rescue (Figure 6G). This suggested that MBD was required for correct chromocenter clustering, whereas TRD was dispensable for this process.

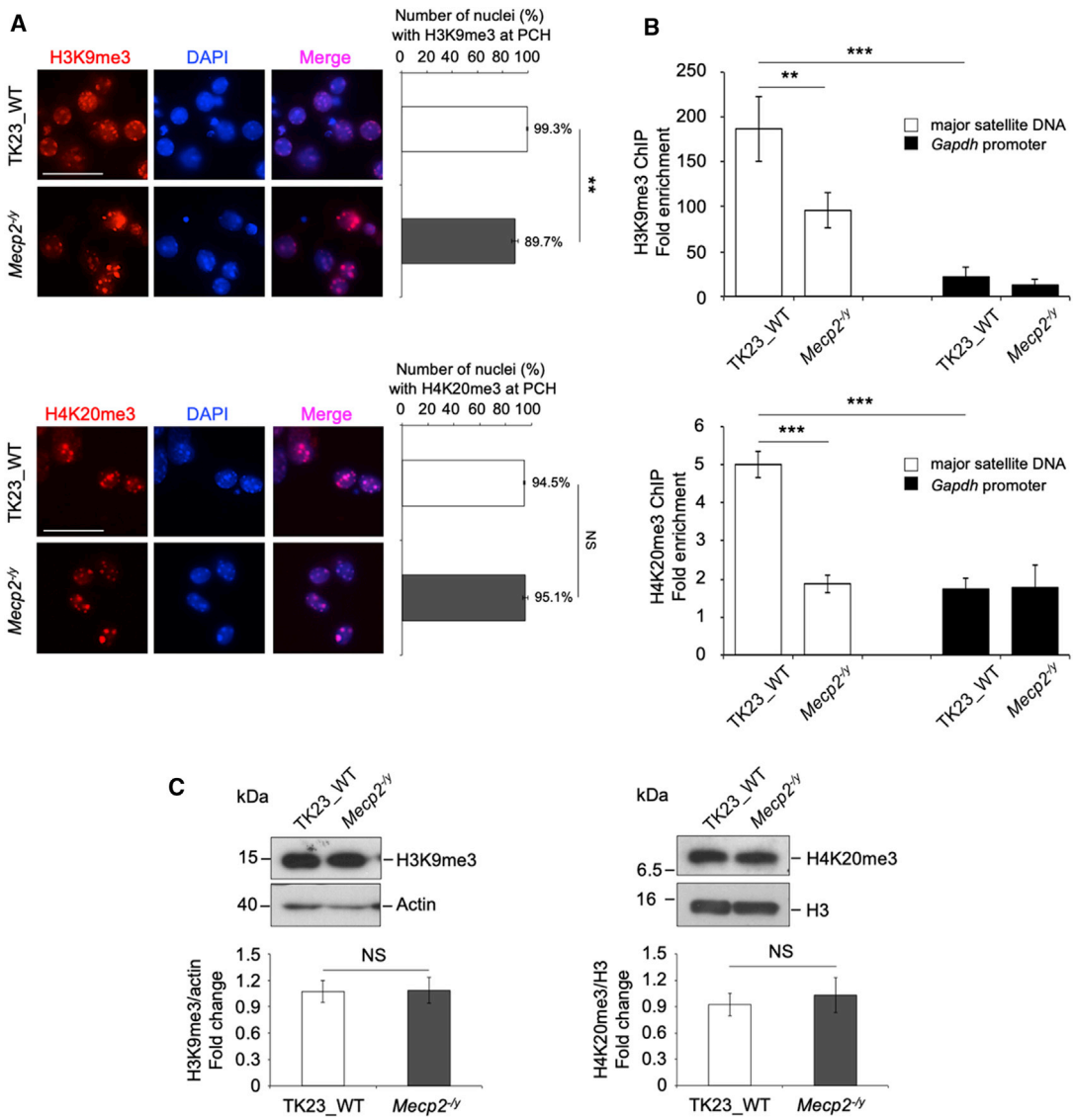

Figure 5. H3-Lys9 and H4-Lys20 Trimethylation Is Lower in Terminally Differentiated *Mecp2*-null Neurons

(A) Left: Representative immunofluorescence of H3K9me3 and H4K20me3 marks in terminally differentiated TK23_WT and *Mecp2*$^{-/y}$ neurons. Chromocenters were stained with DAPI. Scale bars, 25 μm. Right: Quantification of H3K9me3 and H4K20me3 enrichment at chromocenters in TK23_WT and *Mecp2*$^{-/y}$ nuclei. Data are means ± SD, with ≥100 nuclei analyzed for each cell line, from three independent experiments. **p < 0.01; NS, not significant (one-tailed Student's t test).

(B) ChIP–qPCR of H3K9me3 and H4K20me3 marks at *MajSat* DNA and *Gapdh* promoter (negative control region) in mESC-derived TK23_WT and *Mecp2*$^{-/y}$ neurons. Data are means ± SD of four independent qPCR replicates from two ChIP experiments. ***p < 0.001; **p < 0.01 (one-tailed Student's t test).

(C) Top: Western blots of H3K9me3 and H4K20me3 marks in mESC-derived TK23_WT and *Mecp2*$^{-/y}$ neurons. Actin and histone H3 were used for normalization. Bottom: Quantification of H3K9me3 and H4K20me3 protein expression. Data are means ± SD for H3K9me3/actin and H4K20me3/H3 ratios, with *Mecp2*$^{-/y}$ neurons normalized to TK23_WT neurons, from three independent experiments. NS, not significant (one-tailed Student's t test).

Next, we dissected out the role of the different MeCP2 isoforms and of their two main domains in the targeting of the *MajSat-fw* RNA to PCH, by performing i3D-RNA FISH in the terminally differentiated TK23_WT, *Mecp2*$^{-/y}$, *Mecp2*$^{-/y}$_MeCP2A, *Mecp2*$^{-/y}$_MeCP2B, *Mecp2*$^{-/y}$_MeCP2B_ΔMBD, and *Mecp2*$^{-/y}$_MeCP2B_ΔTRD neurons. As already observed for TK23_WT and *Mecp2*$^{-/y}$ neurons (Figure 2C), in all of these clones, the *MajSat-fw* RNA

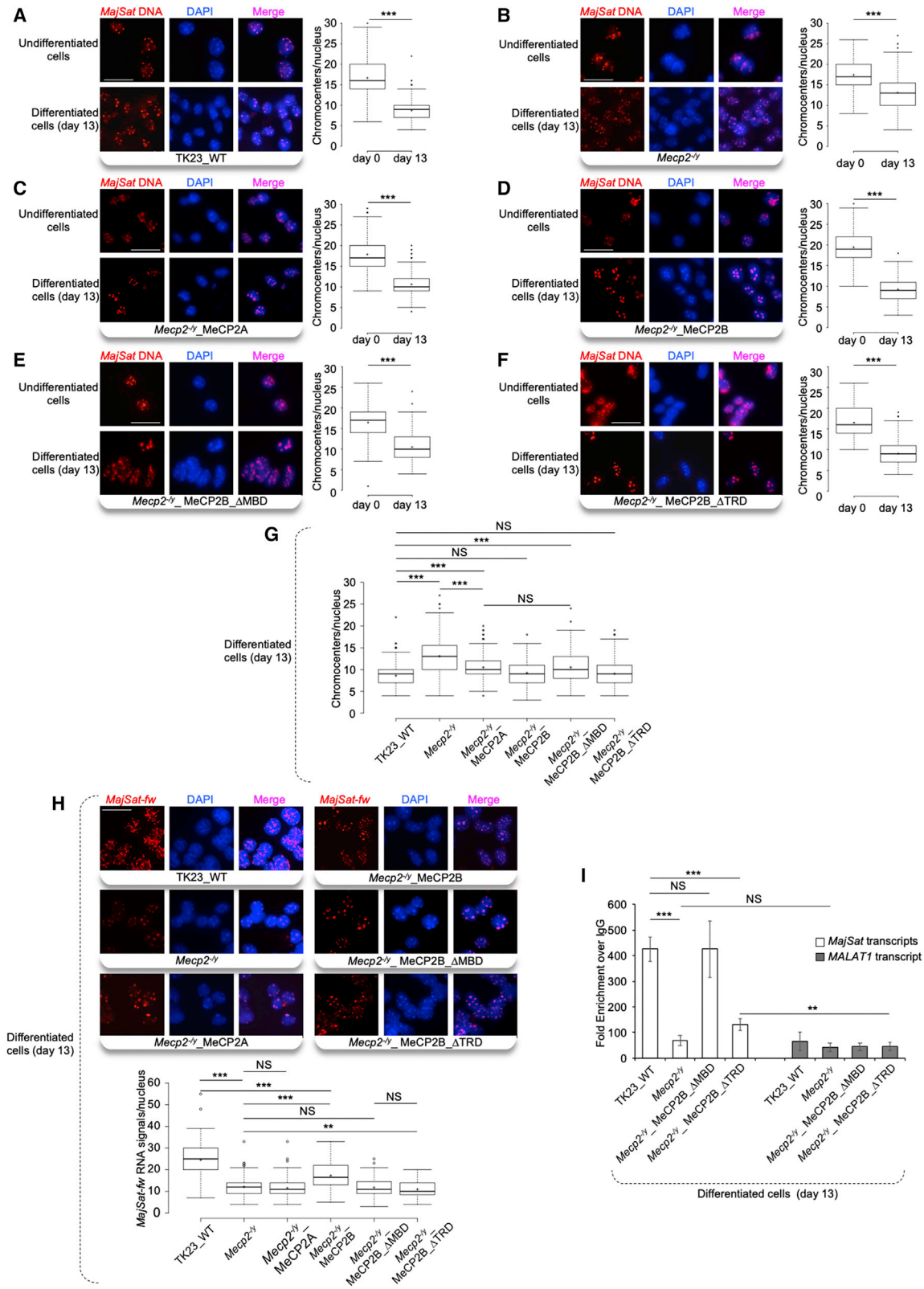

(legend on next page)

predominantly colocalized with chromocenters. *Mecp2*$^{-/y}$_MeCP2A neurons showed fewer spots of *MajSat-fw* RNA associated with PCH as compared with TK23_WT neurons and similar to those of *Mecp2*$^{-/y}$ neurons, whereas *Mecp2*$^{-/y}$_MeCP2B neurons showed an intermediate number between TK23_WT and *Mecp2*$^{-/y}$ neurons. Furthermore, both *Mecp2*$^{-/y}$_MeCP2B_ΔMBD and *Mecp2*$^{-/y}$_MeCP2B_ΔTRD neurons showed similar numbers of RNA signals/nucleus to those for *Mecp2*$^{-/y}$ neurons (Figure 6H). Of note, the number of RNA signals/nucleus in *Mecp2*$^{-/y}$_MeCP2B_ΔTRD neurons was even lower than in *Mecp2*$^{-/y}$ neurons, although this was only a small difference. Altogether, these findings indicated the prevalent contribution of MeCP2B in targeting of *MajSat-fw* transcript to PCH in terminally differentiated neurons, and underlined the involvement of both MBD and TRD in this function. Moreover, native RIP performed in mESC-derived *Mecp2*$^{-/y}$_MeCP2B_ΔMBD and *Mecp2*$^{-/y}$_MeCP2B_ΔTRD neurons revealed that MeCP2B_ΔMBD bound *MajSat* RNAs similar to the WT MeCP2, whereas in the absence of TRD, this interaction was strongly affected, although residual binding was detected (Figure 6I). These data highlighted a key role for TRD in the binding of MeCP2 with *MajSat* RNAs in mESC-derived neurons.

Finally, immunofluorescence showed that MeCP2A, MeCP2B, and MeCP2B_ΔTRD accumulated at chromocenters (Figure S6B), similar to the endogenous MeCP2 protein, although there were small amounts of MeCP2B_ΔTRD in the cell cytoplasm, which might be due to the absence of one nuclear localization signal (Kumar et al., 2008). Conversely, MeCP2B_ΔMBD appeared to be widespread throughout the nucleoplasm, which was broadly confirmed by ChIP, even though residual binding of MeCP2B_ΔMBD to *MajSat* DNA was detected (Figures S6B and S6C).

The RTT Mutation T158M Impairs Chromocenter Clustering and Targeting of the *MajSat-fw* Transcript to PCH

We tested the effects on higher-order PCH organization of two common RTT missense mutations (Neul et al., 2008) located within NID and MBD: R306C and T158M, respectively (Lyst et al., 2013; Nan et al., 1993).

For this, we used *Mecp2*[R306C]^{EGFP}, *Mecp2*[T158M]^{EGFP}, and *Mecp2*[WT]^{EGFP} knock-in mESCs (referred to as R306C-GFP, T158M-GFP, and WT-GFP, respectively) in which the MeCP2 proteins were fused in-frame with EGFP at their C-terminus (Lyst et al., 2013). Importantly, both MeCP2A and MeCP2B were affected by the knock-in.

First, we confirmed that the neural differentiation of R306C-GFP and T158M-GFP was similar to WT-GFP mESCs (Lyst et al., 2013) (Figure S7A). Furthermore, the MeCP2^{WT-GFP} and MeCP2$^{R306C-GFP}$ proteins accumulated at PCH in terminally differentiated neurons, whereas MeCP2$^{T158M-GFP}$ partially lost this chromocenter accumulation, as previously reported (Lyst et al., 2013). Moreover, MeCP2$^{R306C-GFP}$ and MeCP2$^{T158M-GFP}$ protein levels were similar to those of MeCP2^{WT-GFP} (Figure S7B).

Interphase three-dimensional-DNA FISH performed in undifferentiated WT-GFP, R306C-GFP, and T158M-GFP mESCs (day 0) and in terminally differentiated neurons (day 13) highlighted that the *MajSat* DNA distribution overlapped with intense DAPI staining in the nuclei of all of the cell lines (Figures 7A–7C). Comparisons of the numbers of chromocenters/nucleus at day 0 and day 13 for each cell line showed that the chromocenters were clustered in all of these cells (Figures 7A–7C). Nonetheless, when we compared the terminally differentiated neurons with each other, T158M-GFP, but not R306C-GFP, neurons showed a significant defect in chromocenter clustering, as compared with WT-GFP neurons (Figure 7D). Furthermore,

Figure 6. MeCP2B and Its MBD Are the Major Players for Chromocenter Clustering and Both MBD and TRD Contribute to *MajSat-fw* Transcript Targeting to PCH

(A–F) Left: Representative images of i3D-DNA FISH in TK23_WT, *Mecp2*$^{-/y}$, *Mecp2*$^{-/y}$_MeCP2A, *Mecp2*$^{-/y}$_MeCP2B, *Mecp2*$^{-/y}$_MeCP2B_ΔMBD, and *Mecp2*$^{-/y}$_MeCP2B_ΔTRD undifferentiated cells (day 0) and terminally differentiated neurons (day 13) using the *MajSat-fw* LNA probe. Chromocenters were stained with DAPI. Scale bar, 25 μm. Right: Quantification of chromocenters in three-dimensional space of each nucleus in undifferentiated mESCs and terminally differentiated neurons.

(G) Direct comparisons of the data reported in (A–F) for terminally differentiated neurons.

(H) Top: Representative images of i3D-RNA FISH in terminally differentiated TK23_WT, *Mecp2*$^{-/y}$, *Mecp2*$^{-/y}$_MeCP2A, *Mecp2*$^{-/y}$_MeCP2B, *Mecp2*$^{-/y}$_MeCP2B_ΔMBD, and *Mecp2*$^{-/y}$_MeCP2B_ΔTRD neurons, using the *MajSat-fw* LNA probe. Chromocenters were stained with DAPI. Scale bar, 25 μm. Bottom: Quantification of *MajSat-fw* RNA signals in three-dimensional space of each nucleus in terminally differentiated neurons. Data for TK23_WT and *Mecp2*$^{-/y}$ neurons are also reported in Figure 2C. For (A–H), data are shown as box and whisker plots with 200 nuclei analyzed per condition, from two replicate slides. **p < 0.01; ***p < 0.001; NS, not significant (two-sample Kolmogorov-Smirnov test, without (A–F) and with (G, H) Benjamini–Hochberg correction).

(I) RNA immunoprecipitation of *MajSat* transcripts in mESC-derived *Mecp2*$^{-/y}$_MeCP2B_ΔMBD, *Mecp2*$^{-/y}$_MeCP2B_ΔTRD, TK23_WT (positive control), and *Mecp2*$^{-/y}$ (negative control) neurons, using an anti-MeCP2 antibody. Data are means ± SD of three independent qPCR replicates from one representative RIP experiment. Additional biological replicates yielded similar results. ***p < 0.001; **p < 0.01; NS, not significant (one-tailed Student's t test). See also Figures S4–S6.

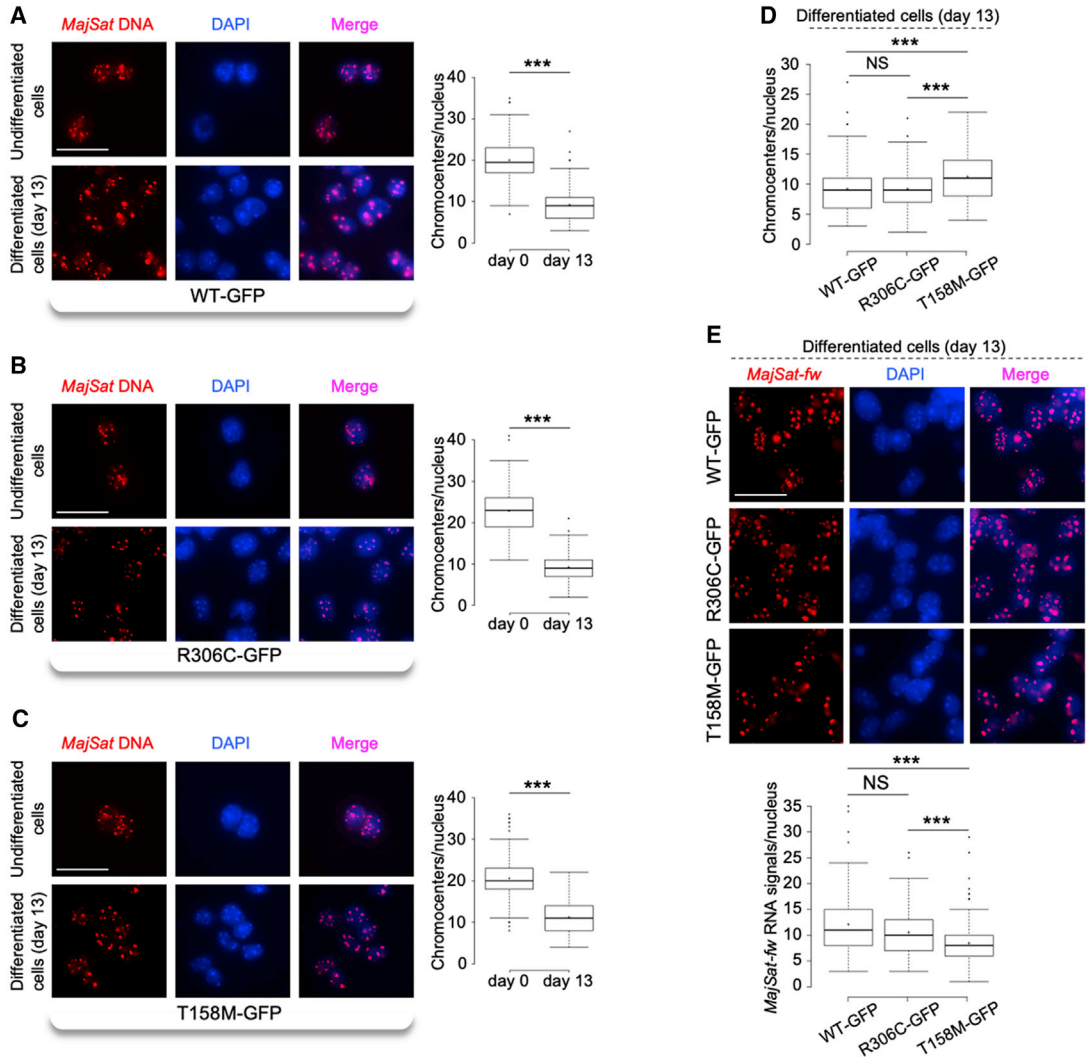

Figure 7. The T158M Mutation Affects Both Chromocenter Clustering and Targeting of the *MajSat-fw* Transcript to Chromocenters

(A–C) Left: Representative images of i3D-DNA FISH in WT-GFP, R306C-GFP, and T158M-GFP undifferentiated cells (day 0) and terminally differentiated neurons (day 13), using the *MajSat-fw* LNA probe. Chromocenters were stained with DAPI. Scale bar, 25 μm. Right: Quantification of chromocenters in three-dimensional space of each nucleus in undifferentiated mESCs and in terminally differentiated neurons.

(D) Direct comparisons of the data reported in (A–C) for terminally differentiated neurons.

(E) Top: Representative images of i3D-RNA FISH in terminally differentiated WT-GFP, R306C-GFP, and T158M-GFP neurons, using the *MajSat-fw* LNA probe. Chromocenters were stained with DAPI. Scale bar, 25 μm. Bottom: Quantification of *MajSat-fw* RNA signals in the three-dimensional space of each nucleus in terminally differentiated neurons. For both i3D-DNA FISH and i3D-RNA FISH, data are shown as box and whisker plots with 200 nuclei analyzed per condition, from two replicate slides. ***$p < 0.001$; NS, not significant (two-sample Kolmogorov-Smirnov test, without (A–C) and with (D, E) Benjamini–Hochberg correction). See also Figure S7.

analysis of the nuclear distribution of *MajSat-fw* RNA by i3D-RNA FISH in mESC-derived R306C-GF, T158M-GFP, and WT-GFP neurons highlighted accumulation of the *MajSat-fw* transcript primarily at PCH in all of the cell lines. Moreover, WT-GFP and R306C-GFP neurons showed similar numbers of RNA signals/nucleus, whereas for T158M-GFP neurons, these were significantly lower (Figure 7E).

Altogether, these data underlined the relevance of the T158 amino acid for both PCH condensation during neural differentiation and targeting of *MajSat-fw* RNA to chromocenters in neurons.

DISCUSSION

Chromocenters appear to form a repressive environment that is enriched in silencing factors that contribute to maintenance of heterochromatic status (Almouzni and Probst, 2011; Wijchers et al., 2015). We previously highlighted a role for MeCP2 in PCH condensation during neural differentiation (Bertulat et al., 2012; Marano et al., 2019), a context of particular interest considering the neurological nature of Rett syndrome. However, the mechanisms underlying higher-order PCH organization in neurons remain unclear.

Several ncRNAs are involved in chromatin silencing, through recruitment of repressive factors to specific genomic regions (Saxena and Carninci, 2011). We show here that MeCP2 targeting to chromocenters in neurons is dependent on an RNA component, as previously reported for other PCH-related proteins (Huo et al., 2020; Maison et al., 2002; Marano et al., 2019). *MajSat* ncRNAs are optimal candidates as partners of MeCP2 in the organization of PCH architecture (Casanova et al., 2013; Maison et al., 2011; Park et al., 2018). We showed that *MajSat-fw* and *MajSat-rv* transcripts are expressed in TK23_WT and *Mecp2*$^{-/y}$ neurons with similar expression levels in the two cell lines, thus excluding any MeCP2-mediated transcriptional regulation. Of note, only the *MajSat-fw* RNA is condensed into spots at chromocenters, as previously reported (Maison et al., 2011), which suggests diffusion of *MajSat-rv* RNA into the nucleoplasm, and that the two strands act independently of each other.

Our data strongly suggest that MeCP2 and the *MajSat-fw* transcript are mutually dependent for their targeting to chromocenters in neurons. In the absence of MeCP2, there were fewer spots of *MajSat-fw* RNA associated with PCH at each time of neural differentiation, in comparison with the WT condition, which suggested a contribution of MeCP2 in *MajSat-fw* RNA targeting to PCH. Considering the unchanged levels of *MajSat-fw* transcript between TK23_WT and *Mecp2*$^{-/y}$ cells, we hypothesized intranuclear diffusion of part of this transcript in the MeCP2-deficient cells. Furthermore, the *MajSat-fw* transcript knock-down in terminally differentiated TK23_WT neurons strongly reduced the accumulation of MeCP2 at chromocenters, despite unchanged *MajSat* DNA methylation. In addition, MeCP2 binds *MajSat* transcripts, as reported for HP1α and SAFB (Huo et al., 2020; Maison et al., 2011), and according to the interactions of MeCP2 with RNA (Maxwell et al., 2013). These findings allow hypothesis of a direct role for the *MajSat-fw* transcript in MeCP2 targeting to PCH, although we cannot rule out the involvement of additional factors.

We highlighted a reduction in H3K9me3 and H4K20me3 deposition to PCH in the absence of MeCP2, without any consequent increase in *MajSat* expression. We believe that decreased accumulation of the *MajSat-fw* transcript at PCH caused by MeCP2 depletion leads to defective recruitment of Suv39h and suppressor of variegation 4-20 homolog (Suv4-20h) histone methyltransferases (HMTs), and then to reduced H3K9me3 and H4K20me3 deposition at chromocenters. This hypothesis is in agreement with the contribution of satellite RNAs for targeting Suv39h to PCH (Velazquez Camacho et al., 2017). Alternatively, MeCP2 might directly recruit HMTs to PCH, in line with the known interplay between MeCP2 and HMTs (Fuks et al., 2003; Lehnertz et al., 2003).

Overall, these data underlined an important contribution of satellite transcripts in higher-order PCH organization in neurons. We hypothesize that MeCP2 and *MajSat-fw* RNA might cooperate for the organization of silent compartments, by acting as structural organizing factors. In support of this, *MajSat* RNAs have been linked to *de novo* chromocenter formation (Casanova et al., 2013; Probst et al., 2010).

At present, the redundancy of MeCP2A and MeCP2B isoforms is still controversial (Jugloff et al., 2008; Kerr et al., 2012). We highlighted that MeCP2B is the major player for both chromocenter clustering and *MajSat-fw* RNA targeting to PCH during neural differentiation. MeCP2B expression in the *Mecp2*-null context was indeed sufficient to rescue the chromocenter clustering, whereas MeCP2A induced only partial PCH condensation. In addition, MeCP2B expression partly recovered targeting of the *MajSat-fw* RNA to PCH, whereas MeCP2A-expressing cells showed similar defects in RNA accumulation to those in *Mecp2*-null neurons. Nevertheless, the incomplete rescue of RNA targeting in the MeCP2B-expressing cells suggested a small, but significant, contribution of MeCP2A.

Recent data have underlined the relevance to RTT pathogenesis of MBD and NID (Tillotson et al., 2017). MBD promotes binding of MeCP2 to PCH (Brero et al., 2005; Kumar et al., 2008), whereas TRD mediates transcriptional silencing (Lyst et al., 2013); however, their roles in higher-order PCH organization remain to be better clarified. We show that MBD is required for chromocenter clustering during neural differentiation, whereas TRD appears to be dispensable, as previously observed in myoblasts (Brero et al., 2005). Interestingly, the similar defect of chromocenter clustering in MeCP2B_ΔMBD or MeCP2A-expressing cells indicated comparable relevance of MBD and the MeCP2B N-terminus in PCH condensation. Furthermore, *MajSat-fw* RNA targeting to PCH is impaired in the absence of MBD or TRD, which underlines the relevance of both of these domains in this process. Our data support the inclusion of a *MajSat* RNA binding site in TRD. Thus, we hypothesize that MeCP2B_ΔTRD binds chromocenters and promotes their clustering, while the

lack of the *MajSat* RNA binding site is responsible for reduced targeting of *MajSat-fw* RNA to PCH. Conversely, the impairment of both chromocenter clustering and targeting of *MajSat-fw* RNA to PCH in MeCP2B_ΔMBD-expressing neurons might be ascribed to the strongly reduced interaction with the heterochromatic foci, even though the binding of the transcript is preserved.

Some MeCP2 RTT mutations affect its DNA-binding capacity and chromatin-binding kinetics (Agarwal et al., 2011; Kumar et al., 2008). However, whether the alterations in chromatin structure derived from MeCP2 defects contribute to RTT pathogenesis remains unclear. We show that the T158M, but not the R306C, mutation moderately impairs both chromocenter clustering and *MajSat-fw* RNA targeting to PCH. These defects might be due to partial delocalization of MeCP2$^{T158M-GFP}$ from PCH, considering that the T158M mutation reduces its affinity for DNA (Ho et al., 2008). We hypothesize that the fraction of MeCP2$^{T158M-GFP}$ bound to PCH is responsible for both partial chromocenter clustering and *MajSat-fw* RNA targeting to PCH.

Overall, these data underline the importance of the T158 amino acid in higher-order PCH organization, as observed for MBD.

In conclusion, it is tempting to speculate that defects in PCH organization caused by MeCP2 alterations are responsible for inappropriate localization of specific genes with respect to silent compartments. This might give rise to their incorrect expression, which will have a pathogenic role in RTT. However, further studies are needed to more clearly correlate alterations of higher-order PCH organization and the RTT-related phenotype.

EXPERIMENTAL PROCEDURES

Antisense LNA Gapmer Transfection

mESC-derived WT neurons were transfected with 10 nM LNA gapmer *MajSat-fw*-6FAM (Exiqon), TK23_WT neurons were transfected with 25 nM–300 nM LNA gapmer *MajSat-fw* or the negative control A gapmer (scrambled) (Exiqon), using Lipofectamine RNAiMax (Life Technologies), according to the manufacturer's protocol. Twelve hours after transfection, the medium was replaced, and after a further 12 h, the cells were collected.

Interphase Three-Dimensional-DNA FISH

Cells were fixed with 4% paraformaldehyde (PFA) for 10 min, permeabilized with 0.2% Triton X-100/PBS for 10 min, and stored in 75% ethanol overnight at 4°C. Following dehydration in 90% and 100% ethanol, and denaturation in 2× saline sodium citrate buffer (SSC), 50% formamide (Sigma-Aldrich) at 80°C for 30 min, hybridization was carried out with 0.1 μM major 1 LNA fluorescent probe (Exiqon) (Probst et al., 2010) in 30% formamide, 1.6 mg/mL salmon sperm DNA (Sigma-Aldrich), 10% dextran sulfate (Fluka), 1 mg/mL BSA, 2× SSC, for 35 min at 37°C. After three washes in 0.1× SSC for 5 min at 60°C, the slides were mounted using Vectashield (Vector Laboratories)/DAPI.

Interphase Three-Dimensional-RNA FISH and Immuno-RNA FISH

nterphase three-dimensional-RNA FISH was performed as previously reported (Maison et al., 2011). Briefly, cells were permeabilized with 0.5% Triton X-100/CSK buffer (10 mM Pipes, pH 7, 100 mM NaCl, 300 mM sucrose, 3 mM $MgCl_2$) supplemented with 10 mM vanadyl ribonucleoside complex (VRC; New England Biolabs) for 5 min on ice, washed with CSK buffer and PBS. For RNase A treatment, there was an additional incubation with 1 mg/mL RNase A (Roche)/PBS or PBS (mock) for 10 min at room temperature. Cells were fixed with 3% PFA for 12 min and stored in 70% ethanol overnight at −20°C. Following dehydration with 80%, 95%, and 100% ethanol, cells were incubated with 0.2 μM major 1 or major 2 LNA fluorescent probes (Exiqon) (Probst et al., 2010) in 50% formamide, 10% dextran sulfate, 2 mg/mL BSA, 10 mM VRC, 2× SSC, for 35 min at 37°C. After three washes in 0.1× SSC for 5 min at 60°C, the slides were mounted using Vectashield/DAPI.

Immuno-RNA FISH was performed as previously reported (Chaumeil et al., 2002), with minor changes. Briefly, cells were fixed with 3% PFA for 10 min, washed with PBS and CSK buffer, permeabilized with 0.5% Triton X-100/CSK buffer supplemented with 2 mM VRC for 5 min on ice, and washed with CSK buffer and PBS. After blocking with 10% normal goat serum, 1% BSA, 0.4 U RNaseOUT (Life Technologies) in PBS for 15 min, the cells were incubated with the anti-MeCP2 antibody (Table S3) in blocking solution for 45 min.

After washes in PBS, the cells were incubated with the secondary antibody (Alexa Fluor 488 donkey anti-rabbit; Thermofisher Scientific). The cells were then post-fixed in 3% PFA for 10 min, washed with 2× SSC, and incubated with 0.4 μM major 1 LNA fluorescent probe in 30% formamide, 1.6 mg/mL salmon sperm DNA, 10% dextran sulfate, 1 mg/mL BSA, 20 mM VRC, 2× SSC, for 35 min at 37°C. After three washes in 0.1× SSC for 5 min at 60°C, the slides were mounted using Vectashield/DAPI.

Sequence of Primers, Probes, and Gapmers

The sequences of the primers, LNA fluorescent probes, and antisense LNA gapmers used in this study are provided in Tables S1 and S2.

Microscopy and Image Analysis

For all imaging experiments, except for FRET, the images were captured with a fluorescence microscope (DM6000B; Leica) run with the LAS AF 2.6 software (Leica), using a ×63 (NA1.4) objective lens (Leica) and a digital camera (DFC 360FX; Leica).

The proportions of nuclei with MeCP2, H3K9me3, and H4K20me3 enrichment at chromocenters were obtained by analyzing different focal planes along the z axis. For i3D-DNA FISH and i3D-RNA FISH, multichannel z stack images were acquired with a step size of 0.18 μm with the LAS AF 2.6 software, and then the chromocenters (for i3D-DNA FISH) and RNA signals (for i3D-RNA FISH) per nucleus were manually counted along the z axis. The RStudio software was used to generate the box plots. For

immuno-RNA FISH, multichannel z stack images were acquired with a step size of 0.18 μm, and then subjected to deconvolution using the LAS AF 2.6 software.

Nuclei of undifferentiated cells were selected at random, and the analysis of mESC-derived neurons was performed on cells with a neuronal morphology.

Statistical Analysis

For the i3D-DNA FISH and i3D-RNA FISH experiments, statistical analysis was carried out using two-sample Kolmogorov-Smirnov test without or with Benjamini–Hochberg correction (for multiple comparisons). Data are shown as box and whisker plots, where the whiskers show the 5%–95% percentiles of the confidence intervals, the horizontal lines within each box show the medians, the crosses indicate the means, and outliers are shown as dots.

For the Western blot reported in Figure S6A, one-way ANOVA followed by Tukey *post-hoc* test was applied. For all of the other experiments, one-tailed or two-tailed paired Student's t tests were used, as reported in the Figure legends. One-tailed paired Student's t test was used when unidirectional changes were expected. Data are presented as means ± SD (for all experiments, except for FRET assay) or as means ± SEM (for FRET). p values <0.05 are considered significant.

SUPPLEMENTAL INFORMATION

Supplemental Information can be found online at https://doi.org/10.1016/j.stemcr.2020.11.006.

AUTHOR CONTRIBUTIONS

F.D.R. conceived the study; F.D.R., M.D.E, S.F., E.C., and D.M. planned and designed the experiments with the help of M.R.M.; A.B. helped in the earlier experimental phase; F.M. and M.M. managed the animal colonies; F.D.R, S.F., E.C., D.M., C.Z., and A.R. performed the experiments; F.D.R. and S.F. wrote the manuscript with the help of D.M.; M.D.E. and M.R.M. gave conceptual advice and edited the manuscript; all of the authors have reviewed and approved the final manuscript.

CONFLICT OF INTERESTS

The authors declare no competing interests.

ACKNOWLEDGMENTS

The authors are grateful to Prof. Bird and Dr. J. Selfridge for providing the *Mecp2*[WT]^{EGFP}, *Mecp2*[R306C]^{EGFP}, and *Mecp2*[T158M]^{EGFP} knock-in mESCs; Dr. C. Schanen for providing the MTmmMeCP2AEGFP and MTmmMeCP2BEGFP plasmids; Dr. S. Filosa for providing assistance for the generation of the mESC stable clones'; Dr. I. De Feis and M. Gagliardi for statistical suggestions; and Dr. C. Berrie for scientific English editing of the manuscript. They also thank the Integrated Microscopy Facility of IGB-CNR and the Advanced Light Microscopy Facility of CEINGE. This work was supported by the Epigenomics Flagship Project (EPIGEN) MIUR-CNR, Italy; the UE Initial Training Network Project 'DISCHROM' (238242), European Union; the Jérôme Lejeune Foundation (1545), France; the Project MIUR PON03_PE00060_7, Italy; the RETT Italian Association (AIRETT, National Grant 2019), Italy; and the Project PON/MISE 2014-2020 FESR F/050011/01-02/X32, Italy.

Received: May 20, 2020
Revised: November 7, 2020
Accepted: November 10, 2020
Published: December 8, 2020

REFERENCES

Agarwal, N., Becker, A., Jost, K.L., Haase, S., Thakur, B.K., Brero, A., Hardt, T., Kudo, S., Leonhardt, H., and Cardoso, M.C. (2011). MeCP2 Rett mutations affect large scale chromatin organization. Hum. Mol. Genet. *20*, 4187–4195.

Almouzni, G., and Probst, A.V. (2011). Heterochromatin maintenance and establishment: lessons from the mouse pericentromere. Nucleus *2*, 332–338.

Amir, R.E., Van den Veyver, I.B., Wan, M., Tran, C.Q., Francke, U., and Zoghbi, H.Y. (1999). Rett syndrome is caused by mutations in X-linked MECP2, encoding methyl-CpG-binding protein 2. Nat. Genet. *23*, 185–188.

Ben-Shachar, S., Chahrour, M., Thaller, C., Shaw, C.A., and Zoghbi, H.Y. (2009). Mouse models of MeCP2 disorders share gene expression changes in the cerebellum and hypothalamus. Hum. Mol. Genet. *18*, 2431–2442.

Bertulat, B., De Bonis, M.L., Della Ragione, F., Lehmkuhl, A., Milden, M., Storm, C., Jost, K.L., Scala, S., Hendrich, B., D'Esposito, M., et al. (2012). MeCP2 dependent heterochromatin reorganization during neural differentiation of a novel Mecp2-deficient embryonic stem cell reporter line. PLoS One *7*, e47848.

Brero, A., Easwaran, H.P., Nowak, D., Grunewald, I., Cremer, T., Leonhardt, H., and Cardoso, M.C. (2005). Methyl CpG-binding proteins induce large-scale chromatin reorganization during terminal differentiation. J. Cell Biol. *169*, 733–743.

Casanova, M., Pasternak, M., El Marjou, F., Le Baccon, P., Probst, A.V., and Almouzni, G. (2013). Heterochromatin reorganization during early mouse development requires a single-stranded noncoding transcript. Cell Rep. *4*, 1156–1167.

Chahrour, M., Jung, S.Y., Shaw, C., Zhou, X., Wong, S.T., Qin, J., and Zoghbi, H.Y. (2008). MeCP2, a key contributor to neurological disease, activates and represses transcription. Science *320*, 1224–1229.

Chaumeil, J., Okamoto, I., Guggiari, M., and Heard, E. (2002). Integrated kinetics of X chromosome inactivation in differentiating embryonic stem cells. Cytogenet. Genome Res. *99*, 75–84.

D'Esposito, M., Quaderi, N.A., Ciccodicola, A., Bruni, P., Esposito, T., D'Urso, M., and Brown, S.D. (1996). Isolation, physical mapping, and northern analysis of the X-linked human gene encoding methyl CpG-binding protein, MECP2. Mamm. Genome *7*, 533–535.

Della Ragione, F., Vacca, M., Fioriniello, S., Pepe, G., and D'Esposito, M. (2016). MECP2, a multi-talented modulator of chromatin architecture. Brief Funct. Genomics *15*, 420–431.

Dragich, J.M., Kim, Y.H., Arnold, A.P., and Schanen, N.C. (2007). Differential distribution of the MeCP2 splice variants in the postnatal mouse brain. J. Comp. Neurol. *501*, 526–542.

Falk, M., Feodorova, Y., Naumova, N., Imakaev, M., Lajoie, B.R., Leonhardt, H., Joffe, B., Dekker, J., Fudenberg, G., Solovei, I., et al. (2019). Heterochromatin drives compartmentalization of inverted and conventional nuclei. Nature *570*, 395–399.

Fico, A., Manganelli, G., Simeone, M., Guido, S., Minchiotti, G., and Filosa, S. (2008). High-throughput screening-compatible single-step protocol to differentiate embryonic stem cells in neurons. Stem Cells Dev. *17*, 573–584.

Fioriniello, S., Marano, D., Fiorillo, F., D'Esposito, M., and Della Ragione, F. (2020). Epigenetic factors that control pericentric heterochromatin organization in mammals. Genes (Basel) *11*, 595.

Fuks, F., Hurd, P.J., Wolf, D., Nan, X., Bird, A.P., and Kouzarides, T. (2003). The methyl-CpG-binding protein MeCP2 links DNA methylation to histone methylation. J. Biol. Chem. *278*, 4035–4040.

Gianakopoulos, P.J., Zhang, Y., Pencea, N., Orlic-Milacic, M., Mittal, K., Windpassinger, C., White, S.J., Kroisel, P.M., Chow, E.W., Saunders, C.J., et al. (2012). Mutations in MECP2 exon 1 in classical Rett patients disrupt MECP2_e1 transcription, but not transcription of MECP2_e2. Am. J. Med. Genet. B Neuropsychiatr. Genet. *159B*, 210–216.

Guy, J., Hendrich, B., Holmes, M., Martin, J.E., and Bird, A. (2001). A mouse Mecp2-null mutation causes neurological symptoms that mimic Rett syndrome. Nat. Genet. *27*, 322–326.

Ho, K.L., McNae, I.W., Schmiedeberg, L., Klose, R.J., Bird, A.P., and Walkinshaw, M.D. (2008). MeCP2 binding to DNA depends upon hydration at methyl-CpG. Mol. Cell *29*, 525–531.

Huo, X., Ji, L., Zhang, Y., Lv, P., Cao, X., Wang, Q., Yan, Z., Dong, S., Du, D., Zhang, F., et al. (2020). The nuclear matrix protein SAFB cooperates with major satellite RNAs to stabilize heterochromatin architecture partially through phase separation. Mol. Cell *77*, 368–383.e7.

Jugloff, D.G., Vandamme, K., Logan, R., Visanji, N.P., Brotchie, J.M., and Eubanks, J.H. (2008). Targeted delivery of an Mecp2 transgene to forebrain neurons improves the behavior of female Mecp2-deficient mice. Hum. Mol. Genet. *17*, 1386–1396.

Jung, B.P., Jugloff, D.G., Zhang, G., Logan, R., Brown, S., and Eubanks, J.H. (2003). The expression of methyl CpG binding factor MeCP2 correlates with cellular differentiation in the developing rat brain and in cultured cells. J. Neurobiol. *55*, 86–96.

Kerr, B., Soto, C.J., Saez, M., Abrams, A., Walz, K., and Young, J.I. (2012). Transgenic complementation of MeCP2 deficiency: phenotypic rescue of Mecp2-null mice by isoform-specific transgenes. Eur. J. Hum. Genet. *20*, 69–76.

Kishi, Y., Kondo, S., and Gotoh, Y. (2012). Transcriptional activation of mouse major satellite regions during neuronal differentiation. Cell Struct. Funct. *37*, 101–110.

Klose, R., and Bird, A. (2003). Molecular biology. MeCP2 repression goes nonglobal. Science *302*, 793–795.

Kriaucionis, S., and Bird, A. (2004). The major form of MeCP2 has a novel N-terminus generated by alternative splicing. Nucleic Acids Res. *32*, 1818–1823.

Kumar, A., Kamboj, S., Malone, B.M., Kudo, S., Twiss, J.L., Czymmek, K.J., LaSalle, J.M., and Schanen, N.C. (2008). Analysis of protein domains and Rett syndrome mutations indicate that multiple regions influence chromatin-binding dynamics of the chromatin-associated protein MECP2 in vivo. J. Cell Sci. *121*, 1128–1137.

Lehnertz, B., Ueda, Y., Derijck, A.A., Braunschweig, U., Perez-Burgos, L., Kubicek, S., Chen, T., Li, E., Jenuwein, T., and Peters, A.H. (2003). Suv39h-mediated histone H3 lysine 9 methylation directs DNA methylation to major satellite repeats at pericentric heterochromatin. Curr. Biol. *13*, 1192–1200.

Lewis, J.D., Meehan, R.R., Henzel, W.J., Maurer-Fogy, I., Jeppesen, P., Klein, F., and Bird, A. (1992). Purification, sequence, and cellular localization of a novel chromosomal protein that binds to methylated DNA. Cell *69*, 905–914.

Lyst, M.J., Ekiert, R., Ebert, D.H., Merusi, C., Nowak, J., Selfridge, J., Guy, J., Kastan, N.R., Robinson, N.D., de Lima Alves, F., et al. (2013). Rett syndrome mutations abolish the interaction of MeCP2 with the NCoR/SMRT co-repressor. Nat. Neurosci. *16*, 898–902.

Maison, C., Bailly, D., Peters, A.H., Quivy, J.P., Roche, D., Taddei, A., Lachner, M., Jenuwein, T., and Almouzni, G. (2002). Higher-order structure in pericentric heterochromatin involves a distinct pattern of histone modification and an RNA component. Nat. Genet. *30*, 329–334.

Maison, C., Bailly, D., Roche, D., Montes de Oca, R., Probst, A.V., Vassias, I., Dingli, F., Lombard, B., Loew, D., Quivy, J.P., et al. (2011). SUMOylation promotes de novo targeting of HP1alpha to pericentric heterochromatin. Nat. Genet. *43*, 220–227.

Marano, D., Fioriniello, S., Fiorillo, F., Gibbons, R.J., D'Esposito, M., and Della Ragione, F. (2019). ATRX contributes to MeCP2-mediated pericentric heterochromatin organization during neural differentiation. Int. J. Mol. Sci. *20*, 5371.

Martinez de Paz, A., Khajavi, L., Martin, H., Claveria-Gimeno, R., Tom Dieck, S., Cheema, M.S., Sanchez-Mut, J.V., Moksa, M.M., Carles, A., Brodie, N.I., et al. (2019). MeCP2-E1 isoform is a dynamically expressed, weakly DNA-bound protein with different protein and DNA interactions compared to MeCP2-E2. Epigenetics Chromatin. *12*, 63.

Maxwell, S.S., Pelka, G.J., Tam, P.P., and El-Osta, A. (2013). Chromatin context and ncRNA highlight targets of MeCP2 in brain. RNA Biol. *10*, 1741–1757.

Nan, X., Meehan, R.R., and Bird, A. (1993). Dissection of the methyl-CpG binding domain from the chromosomal protein MeCP2. Nucleic Acids Res. *21*, 4886–4892.

Neul, J.L., Fang, P., Barrish, J., Lane, J., Caeg, E.B., Smith, E.O., Zoghbi, H., Percy, A., and Glaze, D.G. (2008). Specific mutations in methyl-CpG-binding protein 2 confer different severity in Rett syndrome. Neurology *70*, 1313–1321.

Park, J., Lee, H., Han, N., Kwak, S., Lee, H.T., Kim, J.H., Kang, K., Youn, B.H., Yang, J.H., Jeong, H.J., et al. (2018). Long non-coding RNA ChRO1 facilitates ATRX/DAXX-dependent H3.3 deposition for transcription-associated heterochromatin reorganization. Nucleic Acids Res. *46*, 11759–11775.

Probst, A.V., Okamoto, I., Casanova, M., El Marjou, F., Le Baccon, P., and Almouzni, G. (2010). A strand-specific burst in transcription of pericentric satellites is required for chromocenter formation and early mouse development. Dev. Cell *19*, 625–638.

Rett, A. (1966). [On a unusual brain atrophy syndrome in hyperammonemia in childhood]. Wien Med. Wochenschr. *116*, 723–726.

Saxena, A., and Carninci, P. (2011). Long non-coding RNA modifies chromatin: epigenetic silencing by long non-coding RNAs. Bioessays *33*, 830–839.

Skene, P.J., Illingworth, R.S., Webb, S., Kerr, A.R., James, K.D., Turner, D.J., Andrews, R., and Bird, A.P. (2010). Neuronal MeCP2 is expressed at near histone-octamer levels and globally alters the chromatin state. Mol. Cell *37*, 457–468.

Tillotson, R., Selfridge, J., Koerner, M.V., Gadalla, K.K.E., Guy, J., De Sousa, D., Hector, R.D., Cobb, S.R., and Bird, A. (2017). Radically truncated MeCP2 rescues Rett syndrome-like neurological defects. Nature *550*, 398–401.

Velazquez Camacho, O., Galan, C., Swist-Rosowska, K., Ching, R., Gamalinda, M., Karabiber, F., De La Rosa-Velazquez, I., Engist, B., Koschorz, B., Shukeir, N., et al. (2017). Major satellite repeat RNA stabilize heterochromatin retention of Suv39h enzymes by RNA-nucleosome association and RNA:DNA hybrid formation. Elife *6*, e25293.

Wijchers, P.J., Geeven, G., Eyres, M., Bergsma, A.J., Janssen, M., Verstegen, M., Zhu, Y., Schell, Y., Vermeulen, C., de Wit, E., et al. (2015). Characterization and dynamics of pericentromere-associated domains in mice. Genome Res. *25*, 958–969.

Stem Cell Reports, Volume *15*

Supplemental Information

MeCP2 and Major Satellite Forward RNA Cooperate for Pericentric Heterochromatin Organization

Salvatore Fioriniello, Eva Csukonyi, Domenico Marano, Arianna Brancaccio, Michele Madonna, Carmela Zarrillo, Alessia Romano, Federico Marracino, Maria R. Matarazzo, Maurizio D'Esposito, and Floriana Della Ragione

Supplemental Information

Figure S1

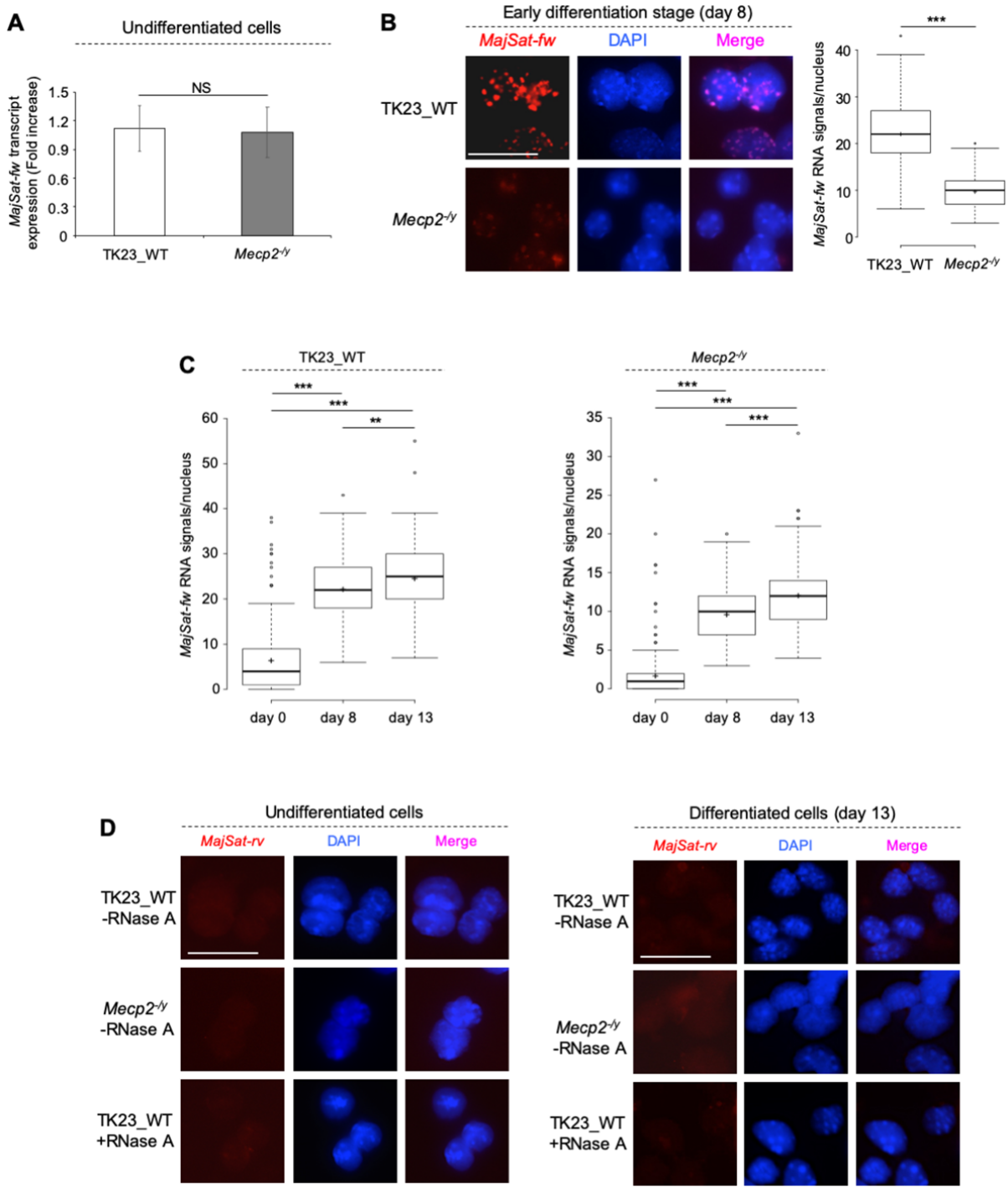

Figure S1. Major satellite forward transcript accumulation at chromocenters progressively increases during neural differentiation (related to Figure 2)

(**A**) Strand-specific RT-qPCR analysis of *MajSat-fw* transcripts in TK23_WT and *Mecp2*$^{-/y}$ undifferentiated cells. Data are normalized to *Gapdh* and are mean ± SD of transcript levels relative to TK23_WT, from three independent experiments. NS, not significant (two-tailed Student's t test).

(**B**) Left: Representative images of i3D-RNA FISH using the *MajSat-fw* LNA probe in TK23_WT and *Mecp2*$^{-/y}$ cells during early stage of neural differentiation (day 8), characterized by the first morphological signs of differentiation (Bertulat et al., 2012). Chromocenters were stained with DAPI. Scale bar, 25 µm. Right: Quantification of *MajSat-fw* RNA signals in 3D space of each nucleus. Data are shown as box and whisker plots with 200 nuclei analyzed per condition, from two replicate slides. ***P<0.001 (two-sample Kolmogorov-Smirnov test).

(**C**) Quantification as for (B) of *MajSat-fw* RNA signals/nucleus in TK23_WT and *Mecp2*$^{-/y}$ cells for undifferentiated state (day 0) and for day 8 and day 13 of neural differentiation. Data are the same reported in Figure 2B and C (day 0 and 13, respectively) and Figure S1B (day 8). Data are shown as box and whisker plots. ***P<0.001; **P<0.01 (two-sample Kolmogorov-Smirnov test with Benjamini-Hochberg correction).
(**D**) Representative images of i3D-RNA FISH using the *MajSat-rv* LNA probe in TK23_WT and *Mecp2*$^{-/y}$ undifferentiated cells and in terminally differentiated neurons. Chromocenters were stained with DAPI. Scale bar, 25 μm.

Figure S2

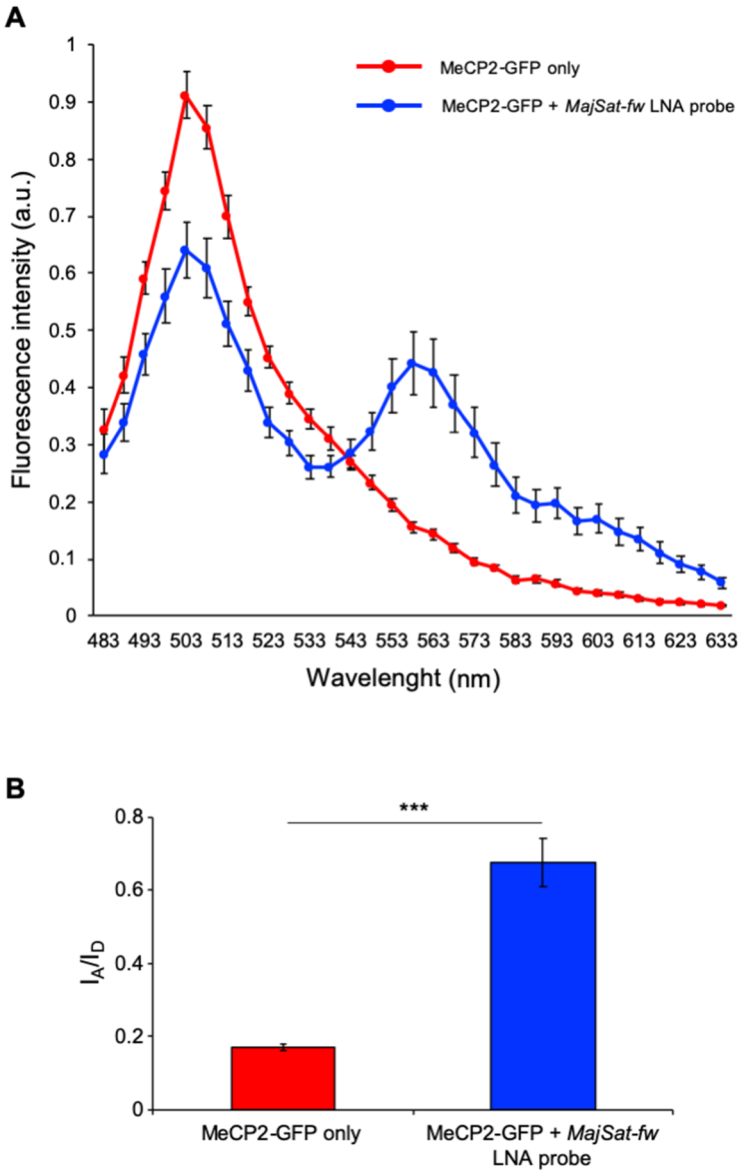

Figure S2. Interaction between MeCP2 and *MajSat-fw* transcript in terminally differentiated neurons analyzed by Fluorescence Resonance Energy Transfer (FRET) (related to Figure 3)

FRET can be observed between the donor EGFP, conjugated to MeCP2 (referred to as MeCP2-GFP), and the acceptor, TYE™563-*MajSat-fw* LNA probe. TYE™563 fluorophore is a direct substitute of Cy3.

(**A**) Emission spectra measured in the presence (MeCP2-GFP + *MajSat-fw* LNA probe) and in the absence (MeCP2-GFP only) of acceptor. λ_{exc}=458 nm. FRET was evaluated measuring fluorescence intensity in the range from 483 to 633 nm after excitation of the donor EGFP (at 458 nm). The occurrence of EGFP-to-TYE™563 FRET in the region of co-localization between MeCP2-GFP and *MajSat-fw* transcript was demonstrated by the decrease of the donor emission peak, at 503 nm, and the concomitant growth of the acceptor emission peak, at 558 nm. Data are mean ± SEM from three independent experiments.

(**B**) FRET ratio calculated as fluorescence intensity of acceptor (IA)/fluorescence intensity of donor (ID), both in the presence (MeCP2-GFP + *MajSat-fw* LNA probe) and in the absence (MeCP2-GFP only) of acceptor. This ratio results strongly and significantly increased in the region of MeCP2-GFP/*MajSat-fw* transcript co-localization. Data are mean ± SEM from three independent experiments; ***P<0.001 (two tailed Student's t test).

Figure S3

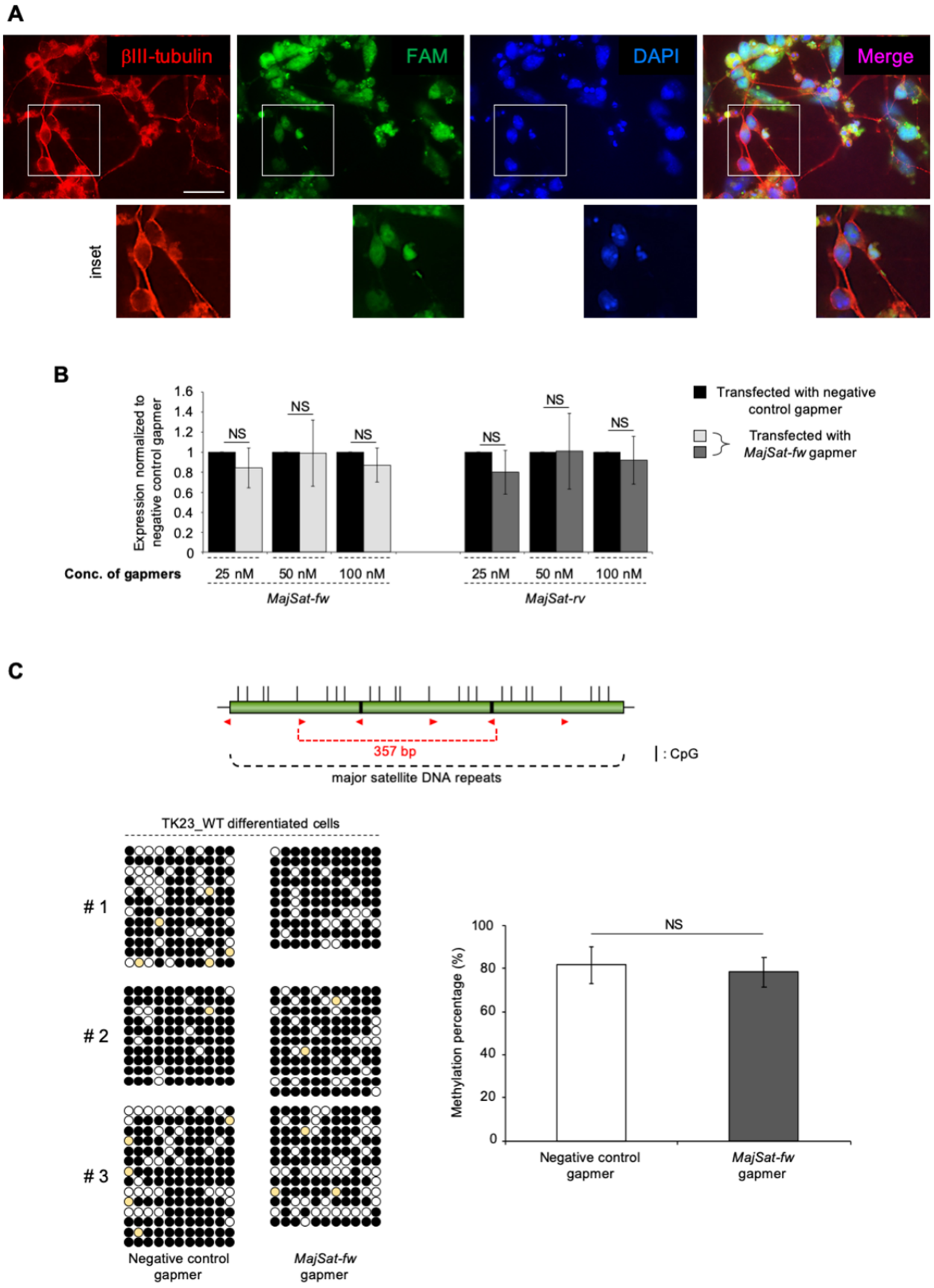
A
βIII-tubulin
FAM
DAPI
Merge
inset
B
Expression normalized to negative control gapmer
1.6
1.4
1.2
1
0.8
0.6
0.4
0.2
0
NS
Conc. of gapmers
25 nM
50 nM
100 nM
MajSat-fw
MajSat-rv
Transfected with negative control gapmer
Transfected with MajSat-fw gapmer
C
357 bp
major satellite DNA repeats
: CpG
TK23_WT differentiated cells
1
2
3
Negative control gapmer
MajSat-fw gapmer
Methylation percentage (%)
100
80
60
40
20
0
NS
Negative control gapmer
MajSat-fw gapmer

Figure S3. Characterization of *MajSat-fw* transcript knock-down in terminally differentiated TK23_WT neurons and analysis of its impact on *MajSat* DNA methylation (related to Figure 4)

(**A**) Representative images of neurons from differentiated WT mESCs (not expressing EGFP), transfected with 10 nM *MajSat-fw* gapmer fluorescently labelled with FAM and analyzed by immunifluorescence. An anti-βIII-tubulin antibody was used to stain neurons. Nuclei were stained with DAPI. Insets: neurons at higher magnification. Scale bar, 25 μm.

(**B**) Strand-specific RT-qPCR analysis of *MajSat-fw* and *MajSat-rv* transcripts in mESC-derived TK23_WT neurons transfected with different amounts of *MajSat-fw* gapmer (concentration relating to medium) and the negative control gapmer (same concentration as for *MajSat-fw* gapmers). Data are normalized to *Gapdh* and are mean ± SD of transcript levels relative to cells transfected with negative control gapmer from three independent experiments. NS, not significant (one-tailed Student's t test).

(**C**) Top: Schematic representation of mouse *MajSat* DNA repeats (green rectangles). Primers used for PCR analysis following bisulfite modification of genomic DNA are depicted by red triangles. Vertical black lines indicate locations of CpGs. Bottom: Bisulfite genomic sequencing analysis of mouse *MajSat* DNA repeats. Left: Bisulfite sequencing pattern analyzed in three biological replicates (indicated by # 1, # 2 and # 3) of terminally differentiated TK23_WT neurons transfected with 300 nM negative control or *MajSat-fw* gapmers. Circles indicate methylation status: black circles represent methylated CpGs; white circles represent unmethylated CpGs; yellow circles indicate no CpG at the expected site. Each row of circles corresponds to one clone. Following bisulfite treatment and PCR, resulting products (357 bp) were cloned and the DNA of at least 10 independent colonies was sequenced. Right: Percentage of total CpG methylation for all samples illustrated in the left panel, is reported as mean ± SD. NS, not significant (two-tailed Student's t test).

Figure S4

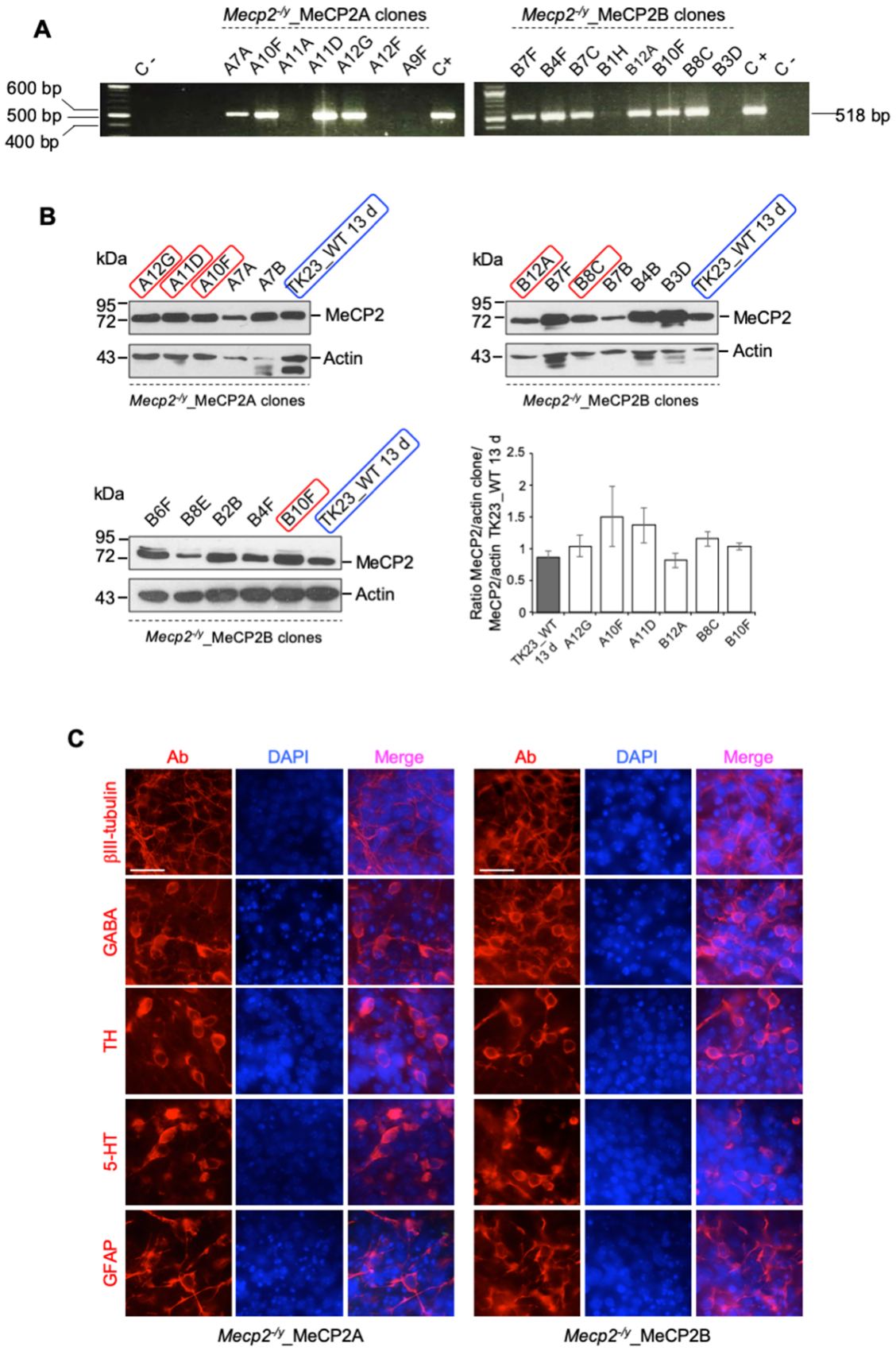
A
Mecp2-/y_MeCP2A clones
Mecp2-/y_MeCP2B clones
C -
A7A
A10F
A11A
A11D
A12G
A12F
A9F
C+
B7F
B4F
B7C
B1H
B12A
B10F
B8C
B3D
C +
C -
600 bp
500 bp
400 bp
518 bp
B
kDa
A12G
A11D
A10F
A7A
A7B
TK23_WT 13 d
95
72
43
MeCP2
Actin
Mecp2-/y_MeCP2A clones
B12A
B7F
B8C
B7B
B4B
B3D
Mecp2-/y_MeCP2B clones
B6F
B8E
B2B
B4F
B10F
Ratio MeCP2/actin clone/ MeCP2/actin TK23_WT 13 d
2.5
2
1.5
1
0.5
0
TK23_WT 13 d
A12G
A10F
A11D
B12A
B8C
B10F
C
Ab
DAPI
Merge
βIII-tubulin
GABA
TH
5-HT
GFAP
Mecp2-/y_MeCP2A
Mecp2-/y_MeCP2B

Figure S4. *Mecp2*$^{-/y}$_MeCP2A and *Mecp2*$^{-/y}$_MeCP2B mESC clones differentiate towards neural fate (related to Figure 6)

(**A**) Representative PCR screening of transfected *Mecp2*$^{-/y}$_MeCP2A and *Mecp2*$^{-/y}$_MeCP2B mESC clones. The 518 bp band indicates insertion of the plasmid containing the coding region of MeCP2A or MeCP2B in the genomic DNA. C+, positive control (plasmid containing coding region of MeCP2A or MeCP2B); C–, negative control.

(**B**) Representative western blot of MeCP2 in *Mecp2*$^{-/y}$_MeCP2A and *Mecp2*$^{-/y}$_MeCP2B mESC clones screened as in (A). The anti-MeCP2 antibody recognizes a portion of the protein downstream of the TRD. Cells expressing MeCP2A or MeCP2B levels comparable to the endogenous protein levels expressed in mESC-derived TK23_WT neurons (loaded as control; blue boxes) were selected (red boxes). Actin was used as normalizer. Quantification of MeCP2A or MeCP2B protein expression in selected clones is reported. Data are mean ± SD from three independent experiments, as MeCP2/actin ratios for each mESC clone normalized to MeCP2/actin ratio of TK23_WT cells. None of the selected clones showed significant differences compared with TK23_WT cells (two-tailed Student's t test).

A12G and B8C clones were selected for the subsenquent experiments.

(**C**) Representative images of immunofluorescence in *Mecp2*$^{-/y}$_MeCP2A and *Mecp2*$^{-/y}$_MeCP2B clones (A12G and B8C, respectively) at day 13. Generation of mature (βIII-tubulin+), GABAergic (GABA+), dopaminergic (tyrosine hydroxylase+; TH+), and serotonergic (5-hydroxytryptamine+; 5-HT+) neurons and astrocytes (glial fibrillary acidic protein+; GFAP+) was assayed. Nuclei were stained with DAPI. Scale bar, 25 μm.

Figure S5

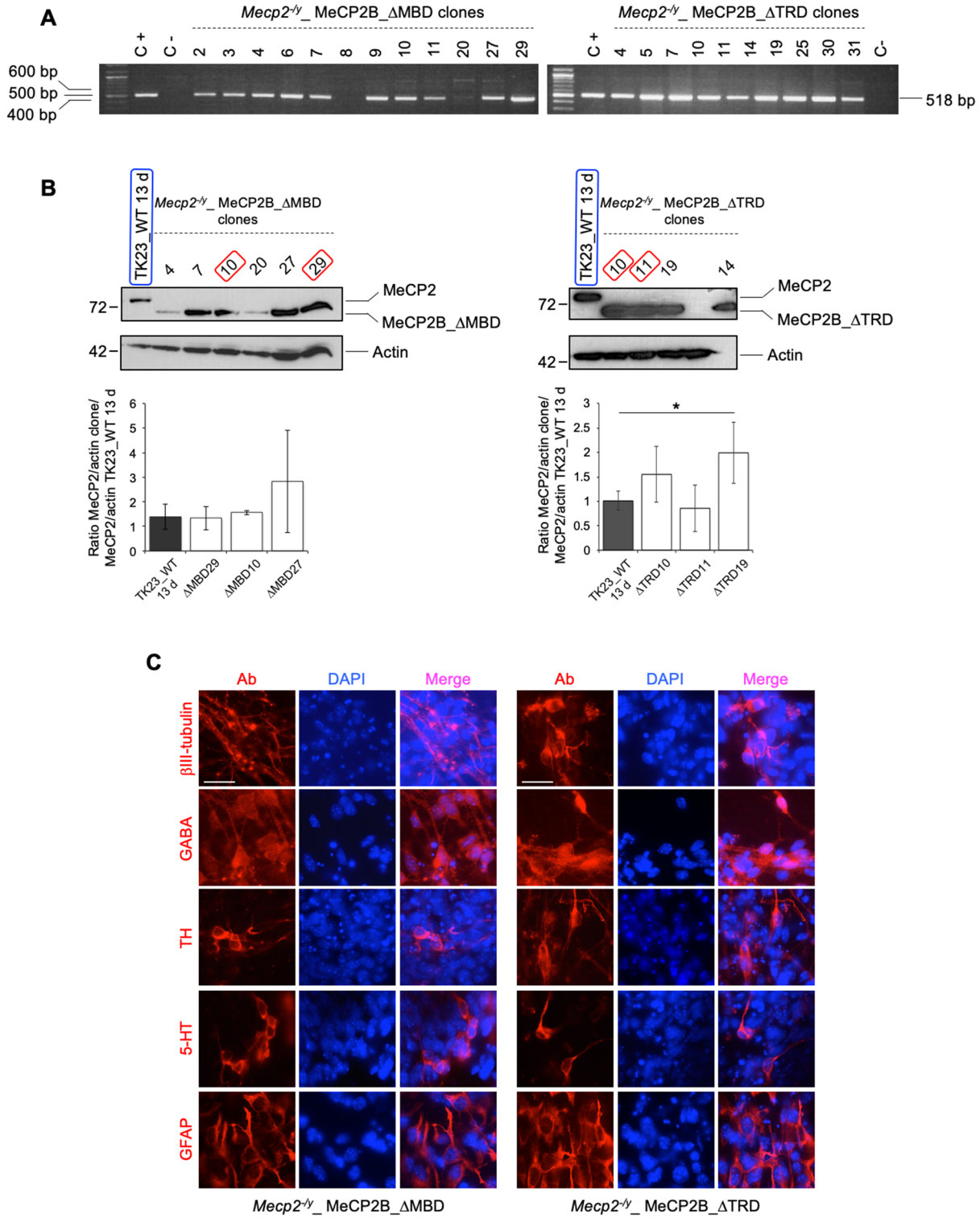
A
Mecp2-/y_ MeCP2B_ΔMBD clones
Mecp2-/y_ MeCP2B_ΔTRD clones
C +
C -
2 3 4 6 7 8 9 10 11 20 27 29
C +
4 5 7 10 11 14 19 25 30 31
C-
600 bp
500 bp
400 bp
518 bp
B
TK23_WT 13 d
Mecp2-/y_ MeCP2B_ΔMBD clones
4 7 10 20 27 29
MeCP2
MeCP2B_ΔMBD
Actin
72
42
Ratio MeCP2/actin clone/ MeCP2/actin TK23_WT 13 d
TK23_WT 13 d
ΔMBD29
ΔMBD10
ΔMBD27
TK23_WT 13 d
Mecp2-/y_ MeCP2B_ΔTRD clones
10 11 19 14
MeCP2
MeCP2B_ΔTRD
Actin
*
TK23_WT 13 d
ΔTRD10
ΔTRD11
ΔTRD19
C
Ab
DAPI
Merge
βIII-tubulin
GABA
TH
5-HT
GFAP
Mecp2-/y_ MeCP2B_ΔMBD
Mecp2-/y_ MeCP2B_ΔTRD

Figure S5. *Mecp2*$^{-/y}$_MeCP2B_ΔMBD and *Mecp2*$^{-/y}$_MeCP2B_ΔTRD mESC clones differentiate towards neural fate (related to Figure 6)

(**A**) Representative PCR screening of transfected *Mecp2*$^{-/y}$_MeCP2B_ΔMBD and *Mecp2*$^{-/y}$_MeCP2B_ΔTRD mESC clones. The 518 bp band indicates the insertion of the plasmid containing the coding region of MeCP2B_ΔMBD or MeCP2B_ΔTRD in the genomic DNA. C+, positive control (plasmid containing coding region of MeCP2B_ΔMBD or MeCP2B_ΔTRD); C–, negative control.

(**B**) Representative western blot of MeCP2 in *Mecp2*$^{-/y}$_MeCP2B_ΔMBD and *Mecp2*$^{-/y}$_MeCP2B_ΔTRD mESC clones screened as in (A). The anti-MeCP2 antibody recognizes a portion of the protein downstream of the TRD. Cells expressing MeCP2B_ΔMBD or MeCP2B_ΔTRD levels comparable to the endogenous protein levels expressed in mESC-derived TK23_WT neurons (loaded as control; blue boxes) were selected (red boxes). Molecular weights of MeCP2B_ΔMBD and MeCP2B_ΔTRD were smaller than endogenous MeCP2 detected in TK23_WT, as expected. Actin was used as normalizer. Quantification of MeCP2B_ΔMBD or MeCP2B_ΔTRD expression in selected clones is reported. Data are means ± SD from three independent experiments, as MeCP2/actin ratios of each mESC clone normalized to MeCP2/actin ratio of TK23_WT cells. *P<0.05 (two tailed Student's t test).

ΔMBD10 and ΔTRD10 clones were selected for the subsenquent experiments.

(**C**) Representative images of immunofluorescence in *Mecp2*$^{-/y}$_MeCP2B_ΔMBD and *Mecp2*$^{-/y}$_MeCP2B_ΔTRD clones (ΔMBD10 and ΔTRD10, respectively) at day 13. Generation of mature (βIII-tubulin+), GABAergic (GABA+), dopaminergic (tyrosine hydroxylase+; TH+) and serotonergic (5-hydroxytryptamine+; 5-HT+) neurons, and astrocytes (glial fibrillary acidic protein+; GFAP+) was assayed. Nuclei were stained with DAPI. Scale bar, 25 μm.

Figure S6

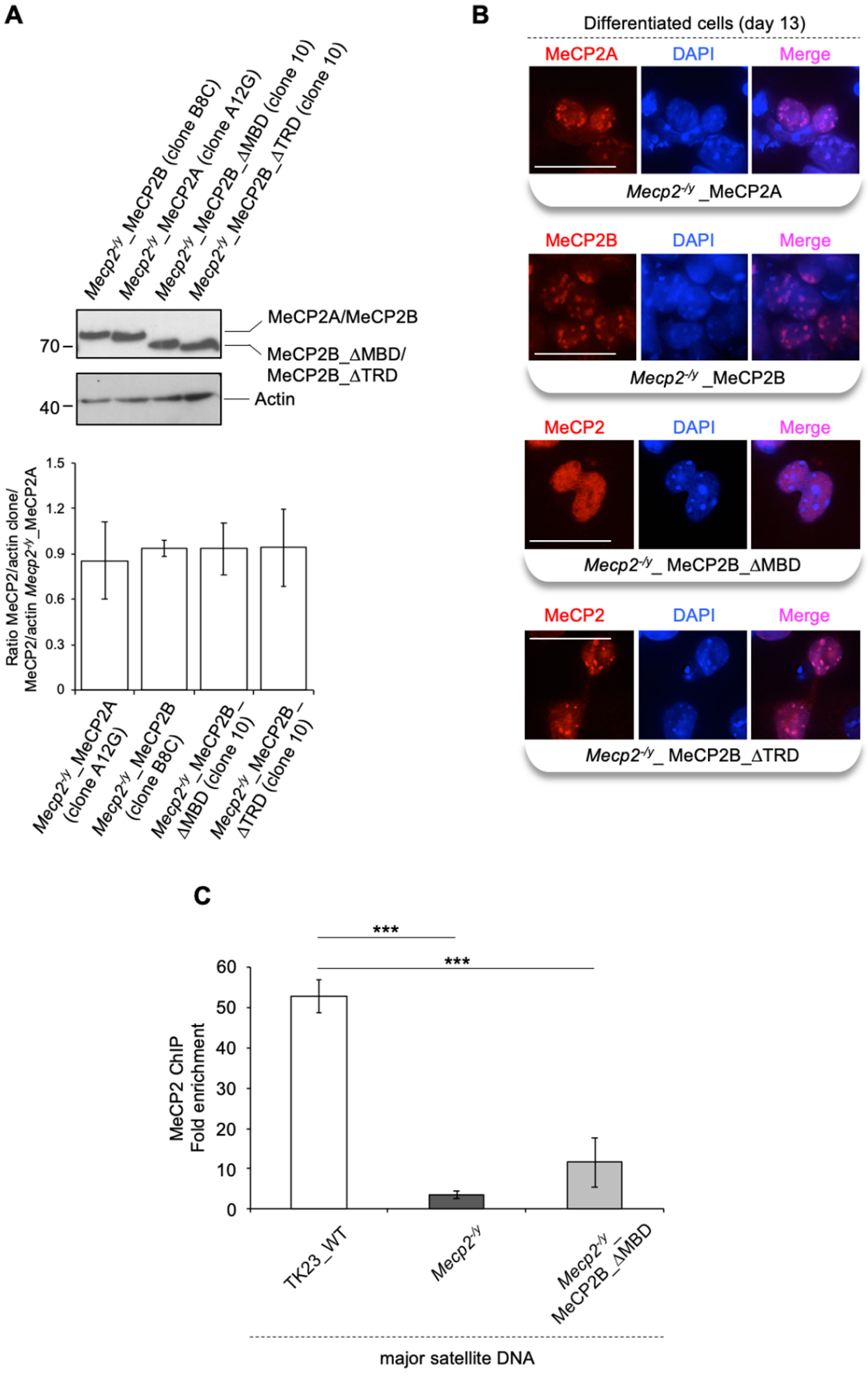
A
Mecp2-/y _MeCP2B (clone B8C)
Mecp2-/y _MeCP2A (clone A12G)
Mecp2-/y _MeCP2B_ΔMBD (clone 10)
Mecp2-/y _MeCP2B_ΔTRD (clone 10)
70
40
MeCP2A/MeCP2B
MeCP2B_ΔMBD/
MeCP2B_ΔTRD
Actin
Ratio MeCP2/actin clone/
MeCP2/actin Mecp2-/y_MeCP2A
1.5
1.2
0.9
0.6
0.3
0
Mecp2-/y _MeCP2A (clone A12G)
Mecp2-/y _MeCP2B (clone B8C)
Mecp2-/y _MeCP2B_ΔMBD (clone 10)
Mecp2-/y _MeCP2B_ΔTRD (clone 10)
B
Differentiated cells (day 13)
MeCP2A
DAPI
Merge
Mecp2-/y _MeCP2A
MeCP2B
DAPI
Merge
Mecp2-/y _MeCP2B
MeCP2
DAPI
Merge
Mecp2-/y_ MeCP2B_ΔMBD
MeCP2
DAPI
Merge
Mecp2-/y_ MeCP2B_ΔTRD
C
***
***
MeCP2 ChIP
Fold enrichment
60
50
40
30
20
10
0
TK23_WT
Mecp2-/y
Mecp2-/y _MeCP2B_ΔMBD
major satellite DNA

Figure S6. Both MeCP2A and MeCP2B isoforms accumulate at PCH and the MeCP2B_ΔMBD deleted protein is widespread in the nucleoplasm (related to Figure 6)

(**A**) Top: Western blot analysis of MeCP2 in *Mecp2*$^{-/y}$_MeCP2A, *Mecp2*$^{-/y}$_MeCP2B, *Mecp2*$^{-/y}$_MeCP2B_ΔMBD and *Mecp2*$^{-/y}$_MeCP2B_ΔTRD selected mESC clones (A12G, B8C, ΔMBD10 and ΔTRD10, respectively). Molecular weights of MeCP2B_ΔMBD and MeCP2B_ΔTRD were smaller than MeCP2 detected in *Mecp2*$^{-/y}$_MeCP2A and *Mecp2*$^{-/y}$_MeCP2B mESC clones, as expected. Actin was used as normalizer. Bottom: Quantification of MeCP2 protein expression in selected clones. Data are means ± SD from three independent experiments, as MeCP2/actin ratios of each mESC clone normalized to MeCP2/actin ratio of *Mecp2*$^{-/y}$_MeCP2A cells. None of the selected clones showed significant differences (one-way ANOVA followed by Tukey post-hoc test).

(**B**) Representative immunofluorescence of MeCP2 in terminally differentiated *Mecp2*$^{-/y}$_MeCP2A, *Mecp2*$^{-/y}$_MeCP2B, *Mecp2*$^{-/y}$_MeCP2B_ΔMBD and *Mecp2*$^{-/y}$_MeCP2B_ΔTRD neurons (A12G, B8C, ΔMBD10 and ΔTRD10, respectively). Chromocenters were stained with DAPI. Scale bar, 25 μm.

(**C**) ChIP-qPCR of MeCP2 at *MajSat* DNA in differentiated *Mecp2*$^{-/y}$_MeCP2B_ΔMBD, TK23_WT (positive control) and *Mecp2*$^{-/y}$ (negative control) neurons. Data are means ±SD of four independent qPCR replicates from two ChIP experiments. ***P<0.001 (one-tailed Student's t test).

The anti-MeCP2 antibody used in the experiments showed in A, B and C recognizes a portion of the protein downstream of the TRD.

Figure S7

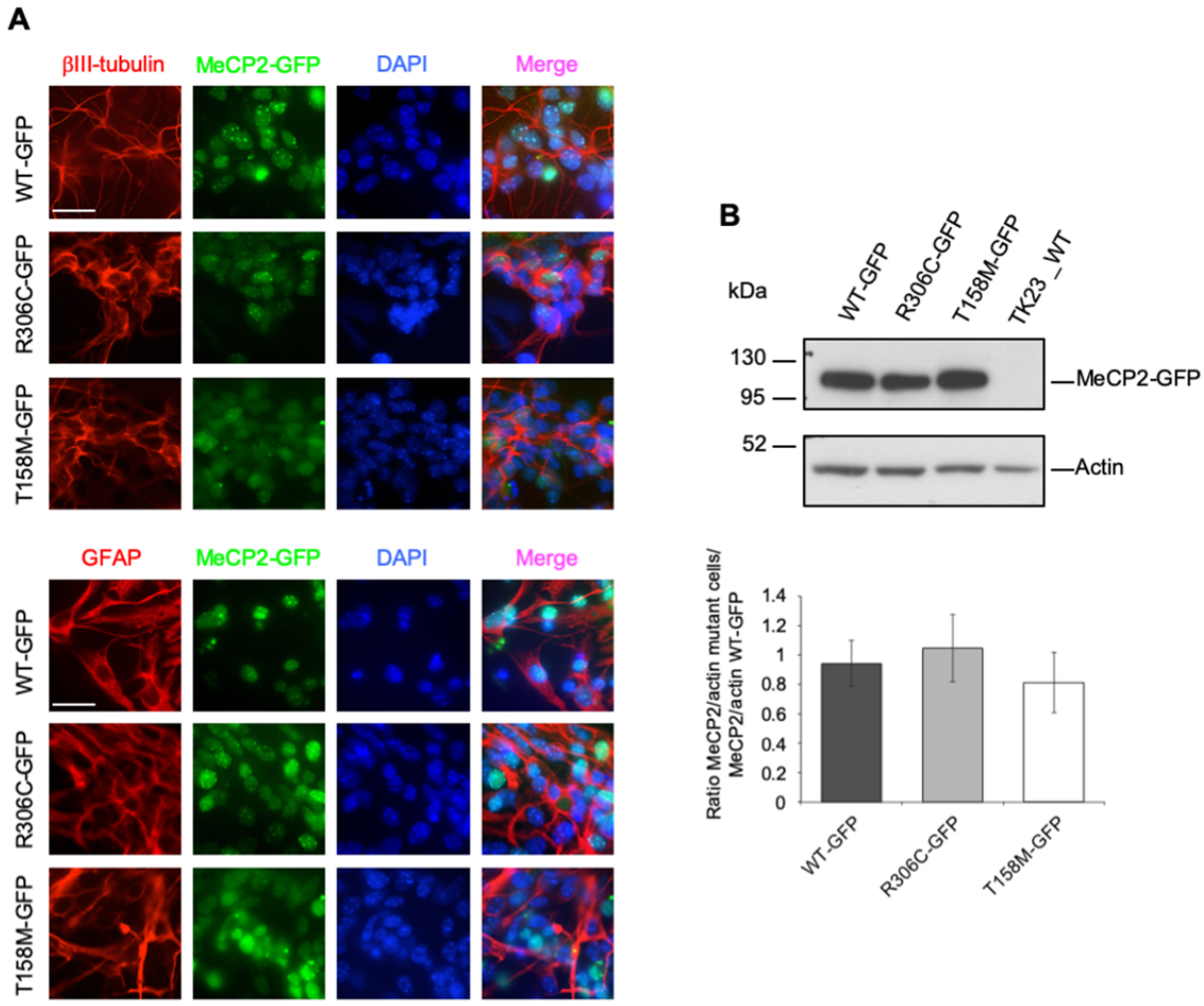

Figure S7. T158M-GFP and R306C-GFP mESCs differentiate towards neural fate as WT-GFP and express similar levels of the MeCP2 protein (related to Figure 7)

(**A**) Representative images of immunofluorescence in terminally differentiated WT-GFP, R306C-GFP and T158M-GFP neurons (day 13). Generation of mature neurons (top: βIII-tubulin+) and astrocytes (bottom: glial fibrillary acidic protein+; GFAP+) was assayed. EGFP (green) highlights wild-type or mutant MeCP2 nuclear localization in WT-GFP, R306C-GFP and T158M-GFP cell lines. Chromocenters were stained with DAPI. Scale bar, 25 μm.

(**B**) Top: Western blot analysis of MeCP2 with anti-EGFP antibody in terminally differentiated WT-GFP, R306C-GFP and T158M-GFP neurons (day 13). mESC-derived TK23_WT neurons are the negative control. Actin was used as normalizer. Bottom: Quantification of $MeCP2^{WT\text{-}GFP}$, $MeCP2^{R306C\text{-}GFP}$ and $MeCP2^{T158M\text{-}GFP}$ protein expression. Data are means ± SD from three independent experiments, as the MeCP2/actin ratios for each mutant cell line normalized to MeCP2/actin ratio of WT-GFP cells. The R306C-GFP and T158M-GFP cell lines did not show significant differences in comparison with WT-GFP cells (two tailed Student's t test).

Table S1. Primers used in this study (related to Figures 1, 2, 3, 4, 5, 6, S1, S3, S4, S5 and S6).

Primer name	Nucleotidic sequence (5'-3')
1A/3A	AAAGAATTCGGCCGGCCATGGCCG
1B	TTTCTGCTCTCTCCTGGSGGGTTCTGGCACTGCTGGGGCGAGCC
2A	CCCTCCAGGAGAGAGCAGAAACCA
2B/4B	AGTGAATTCTCAGCTAACTCTCTCG
3B	TTGACCTCGATGCTGACCGTACCTTCTGATGCTGCTGCCTTTGGT
4A	ACGGTCAGCATCGAGGTCAAGGAA
UP-TGA	CCCACCTAAGAAGGAGCACC
L-pal	GAAGTCAGATGCTCAAGGGGC
major satellites (For)	AAATACACACTTTAGGACG
major satellites (Rev)	TCAAGTGGATGTTTCTCATT
GAPDH F2	ACGGCAAATTCAACGGCACA
GAPDH R2	TCCACGACATACTCAGCACCG
GAPDH prom F2	TGAATGCTGCTTCCCGAGTA
GAPDH prom R2	CTCAACTTTTCCGCAGCCTT
MALAT1 mas1 Forward	GGCTGGGGAGTGTTCCAGTGA
MALAT1 mas1 Reverse	TGGTGGCTGGCACTCCTGGT
Liu_MajSat_fw	GGAATATGGTAAGAAAATTGAAAATTATGG
Liu_MajSat_rv	CCATATTCCAAATCCTTCAATATACATTTC

Table S2. Strand-specific LNA fluorescent probes and antisense LNA gapmers (related to Figures 2, 3, 4, 6, 7, S1 and S2).

LNA fluorescent probes		
Name	**Fluorophore**	**Sequence**
major 1 (specific for MajSat-fw strand) Cat. no. EX500150-27479	TEX 615	TCTTGCCATATTCCACGTCC
major 2 (specific for MajSat-rv strand) Cat. no. EX500150-26917	TEX 615	GCGAGGAAAACTGAAAAAGG
major 3 (specific for MajSat-fw strand) Cat. no. 339406YCO0196697	TYE 563	TCTTGCCATATTCCACGTCC
Antisense LNA gapmers		
Name	**Fluorophore**	**Sequence**
LNA gapmer MajSat-fw ID DESIGN: 531668-1	6FAM	AAGTCGTCAAGTGGAT
LNA gapmer MajSat-fw ID DESIGN: 531668-1	-	AAGTCGTCAAGTGGAT
Negative control A gapmer	-	AACACGTCTATACGC

Table S3. List of antibodies used (related to Figures 1, 3, 4, 5, 6, S3, S4, S5, S6 and S7).

Antibody	Application	Company	Cat. N°
Anti-MeCP2	IF (1:500) WB (1:3500) ChIP (5 µg) RIP (5 µg)	Sigma-Aldrich	M9317
anti-TH (anti-tyrosine hydroxylase)	IF (1:200)	Millipore	AB152
anti-5-HT (anti-5 hydroxytryptamine)	IF (1:200)	Sigma-Aldrich	S5545
anti-GFAP (anti-glial fibrillary acidic protein)	IF (1:300)	Dako Cytomation	Z0334
anti-GABA (anti-γ-aminobutyric acid)	IF (1:400)	Sigma-Aldrich	A2052
anti-βIII-tubulin	IF (1:750)	Sigma-Aldrich	T8660
anti-GFP	WB (1:10000)	Abcam	Ab290
anti-H3K9me3	IF (1:500) WB (1:2500) ChIP (5 µg)	Abcam	Ab8898
anti-H4K20me3	IF (1:500) WB (1:1000) ChIP (5 µg)	Millipore	07-463
anti-actin	WB (1:3500)	Sigma-Aldrich	A2066
anti-histone H3	WB (1:30000)	Abcam	Ab1791

Supplemental Experimental Procedures

Animals

The *Mecp2*$^{tm1.1Bird}$ (*Mecp2*$^{-/y}$) and wild-type C57BL/6J mice were originally from Jackson Laboratories, and were then bred in the Animal Facility at IRCCS Neuromed. Hemizygous mutant males were generated by crossing heterozygous knock-out females with C57BL/6J males. Genotyping was performed by PCR, according to the Jackson Laboratory protocols. All animal experiments were approved by the IRCCS Neuromed Animal Care Review Board and by the Italian Ministry of Health (permit number: 988/2015-PR), and were conducted according to EU Directive 2010/63/EU for animal experiments. Nine-week-old mice (symptomatic and age-matched wild-type) were anaesthetized with ketamine/xylazine injection and sacrificed by cervical dislocation. The brains were removed from the skull and immediately processed for RNA immunoprecipitation.

Plasmids

The coding regions of mouse MeCP2A and MeCP2B were excised by restriction digestion from the MTmmMeCP2AEGFP and MTmmMeCP2BEGFP plasmids, kindly provided by C. Schanen **(**Kumar et al., 2008), and sub-cloned into the pallino βA expression vector (Parisi et al., 2003), under the control of the constitutive chicken β-*actin* promoter. As the coding sequences of MeCP2A and MeCP2B were fused in-frame with EGFP in the original plasmids, TGA stop codons were inserted at the end of the MeCP2 coding sequences. The cloning procedure was performed using standard PCR-based techniques and restriction digestion. The MeCP2B_ΔMBD sequence was created by fusing two PCR products together (ΔMBD-up and ΔMBD-lw). The ΔMBD-up was amplified with 1A/3A and 1B primers and the ΔMBD-lw with 2A and 2B/4B primers. The MeCP2B_ΔTRD sequence was also created by fusing two PCR products (ΔTRD-up and ΔTRD-lw) together. ΔTRD-up was amplified with the 1A/3A and 3B primers and ΔTRD-lw with the 4A and 2B/4B primers. The fused fragments were digested as needed and sub-cloned into the pallino βA expression vector (Parisi et al., 2003), under the control of the chicken β-*actin* promoter. All plasmids were checked by direct sequencing. Primers are listed in Table S1.

Generation and screening of stable mESC clones

The murine embryonic stem cells (mESCs) lacking MeCP2 (tEG) (Bertulat et al., 2012) were electroporated at 250 mV and 500 μF with the linearized pallino βA vector (10 μg) that contained the coding sequences for MeCP2A, MeCP2B, MeCP2B_ ΔMBD or MeCP2B_ΔTRD. After 3 days with 1.5 μg/ml puromycin, the resistant clones were selected, expanded and screened by PCR, using the UP-TGA and L-pal primers (Table S1). The positive clones were analyzed by western blot. The cell lines selected for the experiments had MeCP2 expression similar to the endogenous protein expressed in the terminally differentiated TK23_WT neurons.

Stem cell culture and differentiation

mESCs (all derived from E14 cell line) were cultured without feeder on gelatin (Sigma-Aldrich)-coated plates as previously reported (Bertulat et al., 2012). Neural differentiation was performed as already described (Bertulat et al., 2012: Fico e al., 2008), by cell seeding at 1000 cells/cm^2 (1500 cells/cm^2 for tEG, to compensate for their slower growth). The differentiation medium was Knock-out Dulbecco's minimal essential medium (Life Technologies) supplemented with 15% Knock-out Serum Replacement (Life Technologies), 2 mM L-glutamine, 100 U/ml penicillin/streptomycin, and 0.1 mM 2-mercaptoethanol. The cells were grown for up to 13 days. For i3D-DNA FISH and immunofluorescence for neuronal and glial markers, the mESCs were seeded and differentiated on poly-D-lysine/laminin (both from Sigma-Aldrich)-coated glass slides (Bertulat et al., 2012). For all the other experiments, the cells were plated and differentiated on gelatin-coated plates. For i3D-RNA FISH, immuno-RNA FISH, immunofluorescence for MeCP2, H3K9me3 and H4K20me3, fluorescence resonance energy transfer and antisense LNA gapmer transfection, the cells at an early differentiation stage (day 8, used only for i3D-RNA FISH) and the terminally differentiated neurons were dissociated with Accutase (Sigma-Aldrich), plated at a 1:3 dilution on poly-D-lysine/laminin-coated glass slides, and left to adhere for 24 h, to obtain well separated cells.

Immunofluorescence

For the MeCP2, H3K9me3 and H4K20me3 immunofluorescence, different procedures were applied, according to the required antibodies. For MeCP2 and H3K9me3 immunofluorescence, the cells were fixed in 4% PFA and permeabilized with 0.1% Triton X-100/PBS for MeCP2, or with 0.5% Triton X-100/PBS for H3K9me3. For H4K20me3 immunofluorescence, the cells were washed with CSK buffer (10 mM Pipes, pH 7, 100 mM NaCl, 300 mM sucrose, 3 mM $MgCl_2$) supplemented with protease inhibitors (PI) (Roche), permeabilized with 0.5% Triton X-100/CSK buffer, washed with CSK buffer and PBS, and finally fixed in 2% PFA. For the detection of neuronal (βIII-tubulin, γ-aminobutyric acid, tyrosine hydroxylase, 5-hydroxytryptamine) and glial markers (glial fibrillary acidic protein), the terminally differentiated neurons were fixed in 4% PFA and permeabilized with 0.1% Triton X-100/PBS. Cells were,

then, blocked with 10% normal goat serum (NGS, Agilent)/PBS (for MeCP2, H3K9me3, neuronal and glial markers), or with 2.5% BSA/PBS (for H4K20me3). Then, the cells were incubated with the primary antibodies (i.e., anti-MeCP2, anti-H3K9me3, anti- βIII-tubulin, anti-γ-aminobutyric acid, anti-tyrosine hydroxylase, anti-5-hydroxytryptamine, anti-glial fibrillary acidic protein, anti-H4K20me3). After washes with 0.1% Triton X-100/PBS (for MeCP2, H3K9me3), PBS (for neuronal and glial markers) or 0.1% Tween20/PBS (for H4K20me3), the cells were incubated with the appropriate secondary antibodies (Alexa-Fluor 594 donkey anti-mouse or anti-rabbit; Thermofisher Scientific).
For the immunufluorescence for MeCP2 without or with RNase A treatment, the cells were washed with CSK buffer supplemented with PI, permeabilized with 0.5% Triton X-100/CSK buffer, washed with CSK buffer, with PBS, and then incubated with RNase A (1 mg/ml; Roche)/PBS or with PBS (mock) for 10 min. Then, the cells were fixed with 2% PFA for 10 min. Immunofluorescence for MeCP2 was performed following procedures already described (see above).
The detection of MeCP2 protein has been performed using an anti-MeCP2 antibody that recognizes a portion of the protein downstream of the TRD.
The slides were mounted using Vectashield/DAPI. The quantification of MeCP2, H3K9me3 and H4K20me3 enrichment at chromocenters, represented as proportions of nuclei with MeCP2, H3K9me3 and H4K20me3 spotted to PCH, were obtained by counting at least 200 cells for each condition.
Details of the antibodies are given in Table S3.

Bisulfite sequencing

Genomic DNA was isolated from terminally differentiated TK23_WT neurons transfected with 300 nM LNA gapmer *MajSat-fw* or the negative control A gapmer (Exiqon), using Wizard Genomic DNA Purification Kit (Promega), according to the manufacturer's protocol. Genomic DNA was sonicated in H_2O to obtain fragments of ~500 bp in length, then, 500 ng of DNA were subjected to bisulfite modification using the Epitect Bisulfite kit (Qiagen), according to the manufacturer's protocol. PCR amplification of major satellite DNA was performed by using Liu_MajSat_fw and Liu_MajSat_rv primers (Liu et al., 2013), listed in Table S1. The thermal cycling conditions were: 95 °C for 1 min, followed by 95 °C for 30 s, 60 °C for 30 s and 72 °C for 10 s for 40 cycles. Amplified DNA fragments (357 bp) were extracted from agarose gel using QIAquick Gel Extraction Kit (Qiagen), following the manufacturer's instructions and cloned by using TA cloning kit (Invitrogen). Sequencing of at least 10 clones for each group has been performed by using M13 forward and reverse primers by Eurofins Genomics.

Western blot

Total cell extracts were prepared by resuspending the cells in lysis buffer (100 mM Tris-HCl, pH 8, 140 mM NaCl, 20 mM EDTA, 0.2% SDS, 1% NP-40) supplemented with PI. The extracts enriched in histone proteins were obtained by isolating the nuclei in TEB buffer (0.5% Triton X-100, 0.02% NaN3, in PBS) supplemented with PI, and then with acid extraction with 0.2 N HCl, overnight at 4 °C. Total protein extracts have been used to detect MeCP2 and H3K9me3, whereas extracts enriched of histone proteins were used to analyze H4K20me3. Protein lysates were quantified using the Bradford protein assay (Bio-Rad), separated by SDS-PAGE, and transferred to PVDF membranes. Conventional western blotting assays were performed, by using the primary antibodies listed in Table S3. The detection of MeCP2 protein has been performed using an anti-MeCP2 antibody that recognizes a portion of the protein downstream of the transcriptional repression domain (TRD). Densitometric analysis was performed using the Typhoon Scan and ImageQuant software.

RNA extraction and reverse-transcription qPCR

Total RNA was isolated from mESCs and the terminally differentiated neurons using the QIAzol lysis reagent (Qiagen) and DNase treated with Turbo DNA-freeTM kits (Ambion), according to the manufacturer's instructions. cDNA was obtained by reverse transcription with strand-specific primers for major satellite transcripts [major satellites (For) or (Rev) (Maison et al., 2011)] and for the *Gapdh* transcript (GAPDH R2) (Table S1), using the SuperScript III First-Strand Synthesis system (Life Technologies). Quantitative PCR (qPCR) was performed using the primers for *MajSat* [major satellites (For) and (Rev) (Maison et al., 2011)] and *Gapdh* (GAPDH F2/R2) transcripts (Table S1), with SsoAdvance Universal SYBR Green supermix (Bio-Rad) on a Real Time PCR system (CFX96, Bio-Rad), according to the manufacturer's protocols. The $2^{-\Delta\Delta Cq}$ method was used to determine the relative quantitative levels, and the data were normalized with respect to *Gapdh* expression.

Chromatin immunoprecipitation (ChIP)

All the buffers used for chromatin immunoprecipitation were supplemented with PI. ChIPs were performed as previously described (Skene et al., 2010), with minor changes. Briefly, terminally differentiated neurons were fixed with 1% formaldehyde for 10 min and chromatin was sonicated in ice-cold lysis buffer (1% SDS, 10 mM EDTA, 50 mM Tris-HCl, pH 8.1), to obtain fragments of ~300 bp in length. For ChIP without or with RNase A treatment, the chromatin was incubated with 10 μg RNase A/PBS or with PBS (mock), for 30 min at 37 °C. For ChIP with the anti-MeCP2 and anti-H4K20me3 antibodies, the sheared chromatin was diluted 10-fold in dilution buffer A (1% Triton X-100, 2 mM EDTA, 150 mM NaCl, 20 mM Tris-HCl, pH 8.1) and precleared with protein A-Sepharose (GE-Healthcare); then 5% of the

supernatant was saved as the input. For ChIP with the anti-H3K9me3 antibody, the sonicated chromatin was diluted in dilution buffer B (1% Triton X-100, 0.5 mM EGTA, 140 mM NaCl, 10 mM Tris-HCl, pH 8) and precleared with protein A-Sepharose; then 1% of the supernatant was saved as the input. Appropriate amounts of chromatin were incubated with the anti-MeCP2, anti-H4K20me3 or anti-H3K9me3 antibodies, or with 5 µg normal rabbit IgG antibodies (Millipore). The immunoprecipitated complexes were recovered with protein A-Sepharose and washed with ice-cold buffer, following the different protocols: for ChIP with the anti-MeCP2 and anti-H4K20me3 antibodies, one wash in buffer 1 (0.1% SDS, 1% Triton X-100, 2 mM EDTA, 150 mM NaCl, 20 mM Tris-HCl, pH 8.1), four washes in buffer 2 (0.1% SDS, 1% Triton X-100, 2 mM EDTA, 500 mM NaCl, 20 mM Tris-HCl, pH 8.1), one wash in buffer 3 (250 mM LiCl, 1% NP-40, 1% sodium deoxycholate, 1 mM EDTA, 10 mM Tris-HCl, pH 8.1) and three washes in TE buffer (10 mM Tris-HCl, pH 7.5, 1 mM EDTA); for ChIP with the anti-H3K9me3 antibody, one wash in high-salt buffer (0.1% SDS, 1% NP-40, 0.5% sodium deoxycholate, in PBS) and four washes in wash buffer (500 mM LiCl, 1% NP-40, 1% sodium deoxycholate, 100 mM Tris-HCl, pH 8). The immuno-complexes were then reverse crosslinked, and the DNA was purified and used for qPCR, which was performed with SsoAdvance Universal SYBR Green supermix (Bio-Rad) on a Real Time PCR system (CFX96; Bio-Rad), according to the manufacturer's protocols. Major satellites (For)/(Rev) (Maison et al., 2011) and GAPDH prom F2/R2 were used to amplify the *MajSat* DNA and *Gapdh* promoter (Table S1). Data are expressed as fold-enrichment over background (IgG), which were calculated in terms of $2^{-\Delta\Delta Cq\_ChIP/IgG}$, according to Equations [1] and [2].

$$\Delta Cq = Cq_{IP\ sample\ or\ IgG} - (Cq_{Input} - Log_2\ [input\ dilution\ factor]) \quad [1],$$

$$\Delta\Delta Cq = \Delta Cq_{IP\ sample} - \Delta Cq_{IgG} \quad [2],$$

where Cq is the quantification cycle and the input dilution factor is the fraction of the input chromatin that was saved.
Details of the antibodies used are given in Table S3. The immunoprecipitation of MeCP2 has been performed using an anti-MeCP2 antibody that recognizes a portion of the protein downstream of the TRD.

RNA immunoprecipitation

Native RNA immunoprecipitation (RIP) assays were performed using the Magna RIP RNA Binding Protein Immunoprecipitation kits (Millipore). For the terminally differentiated neurons, RIP was performed according to the manufacturer's instructions. For mouse brain, fresh tissue was finely minced with scalpels and Dounce-homogenized in ice-cold RNase-free PBS, and the cell pellet was processed according to the manufacturer's instructions. Immunoprecipitations were performed with the anti-MeCP2 antibodies (Table S3) or with 5 µg normal rabbit IgG antibodies. The RNA purified from immuno-complexes was reverse transcribed using the SuperScript II First Strand Synthesis system (Life Technologies), and the cDNA was amplified by qPCR, performed with SsoAdvance Universal SYBR Green supermix (Bio-Rad) on a Real Time PCR system (CFX96; Bio-Rad), according to the manufacturer's protocols. *MajSat* and *MALAT1* cDNA were amplified using major satellites (For)/(Rev) (Maison et al., 2011) and MALAT1 mas1 Forward/Reverse (Maxwell et al., 2013) primers, respectively (Table S1). Data are expressed as fold-enrichment over background (IgG), which was calculated in terms of $2^{-\Delta\Delta Cq\_RIP/IgG}$, according to Equations [1] and [2], where input dilution factor is the fraction of the input sample saved.
The immunoprecipitation of MeCP2 has been performed using an anti-MeCP2 antibody that recognizes a portion of the protein downstream of the TRD.

Fluorescence Resonance Energy Transfer

WT-GFP neurons were fixed with 3% PFA for 10 min, washed with PBS and CSK buffer, permeabilized with 0.5% Triton X-100/CSK buffer supplemented with 2 mM VRC for 5 min on ice, washed with CSK buffer and PBS, and stored in 70% ethanol overnight at -20 °C. Following dehydration with 80%, 95% and 100% ethanol, the cells were incubated with 0.2 µM LNA fluorescent probe (Qiagen) (major 3; Table S2) in 50% formamide, 10% dextran sulphate, 2 mg/ml BSA, 10 mM VRC, 2× SSC, for 35 min at 37 °C. After three washes in 2× SSC/50% formamide, pH 7.2 for 5 min at 42 °C and three washes in 2× SSC for 5 min at 42 °C, the slides were mounted using Mowiol (Sigma-Aldrich).
The samples were analyzed with a confocal microscope (Leica SP8 STED3x) run with LasX 3.5 software (Leica), using a 63x (NA1.4) objective lens (Leica). After excitation of the sample with Laser Argon at λ=458 nm, fluorescence emission spectra were registered in xyλ modality in the range between 483 nm and 633 nm in 31 detection steps (bandwidth: 10 nm; stepsize: 5 nm).

Supplemental References

Liu, X., Gao, Q., Li, P., Zhao, Q., Zhang, J., Li, J., Koseki, H., and Wong, J. (2013). UHRF1 targets DNMT1 for DNA methylation through cooperative binding of hemi-methylated DNA and methylated H3K9. Nat Commun 4, 1563.

Parisi, S., D'Andrea, D., Lago, C.T., Adamson, E.D., Persico, M.G., and Minchiotti, G. (2003). Nodal-dependent Cripto signaling promotes cardiomyogenesis and redirects the neural fate of embryonic stem cells. J Cell Biol 163, 303-314.